



Quantification of growth and lateral propagation of the Kashi anticline, southwest Chinese Tian Shan

Jie Chen,¹ Richard Heermance,² Douglas W. Burbank,² Katherine M. Scharer,³ Jijun Miao,^{4,5} and Changsheng Wang¹

Received 11 February 2006; revised 16 January 2007; accepted 2 February 2007; published 28 March 2007.

[1] The Kashi anticline is a north vergent, asymmetric, doubly plunging detachment fold located in the SW Tian Shan foreland. We combine structural, magnetostratigraphic, and topographic data to define the fold's lateral propagation, surface uplift, and concomitant exhumation. Two new magnetostratigraphic sections indicate that the fold began growing at ~ 1.4 Ma and by 1.07 Ma, deformation had propagated eastward ~ 13 km at an average rate of ~ 40 km/Myr. Subsequently, propagation rates increased at least twofold, until the fold reached >60 km in length by 0.8 ± 0.3 Ma. Since then, eastward fold propagation slowed to ~ 15 km/Myr, and the eastern 15–25% of the fold remains buried in the rapidly aggrading foreland. The structure and topography of the emergent fold support interpretations of fold growth in three stages: initial symmetric lateral growth both east and west to a total length of ~ 30 km followed by, first, rapid and, then, slower eastward lengthening to 72 ± 10 km total length. Shortening rates as high as $1.9_{-0.2}^{+0.3}$ mm/yr characterize the western part of the fold but decrease toward the east. Significant dissection of the emergent fold does not occur until topographic relief is sufficient (~ 200 m) to permit stripping of protective conglomerates from across the fold's upper surface. As differential rock uplift continues following breaching of the conglomerate, $\sim 75\%$ of the rock raised above local base level is subsequently eroded at rates as high as 2.4 km/Myr. Despite extensive erosion, the modern fold topography mimics spatial patterns of both long-term shortening and variations in rock uplift.

Citation: Chen, J., R. Heermance, D. W. Burbank, K. M. Scharer, J. Miao, and C. Wang (2007), Quantification of growth and lateral propagation of the Kashi anticline, southwest Chinese Tian Shan, *J. Geophys. Res.*, *112*, B03S16, doi:10.1029/2006JB004345.

1. Introduction

[2] Intracontinental mountain building in convergent settings initiates with the nucleation, growth, and lateral propagation of thrust faults and folds [Armstrong and Oriol, 1965]. These tectonic processes interact with erosion and deposition to create the morphology and the long-term drainage patterns of active convergent regions [Burbank *et al.*, 1999; Gupta, 1997]. Growth of an anticline as a geomorphic entity is driven by an evolving relationship between shortening, rock and surface uplift, sedimentation, and exhumation. In the early phase of folding, rock uplift must outpace exhumation and sedi-

mentation to create a fold morphology; in steady state conditions, these reach an equilibrium, whereas in the final, destructive phase of an fold, exhumation dominates [Daëron *et al.*, 2007; Willett and Brandon, 2002]. Temporal changes in key controlling factors, such as fault geometry, shortening rate, and erosion rate will influence the surface uplift history [e.g., Abbott *et al.*, 1997; Burbank and Anderson, 2001; Burbank, 2002; Whipple *et al.*, 1999]. Because time-dependent changes in these factors are difficult to document, their detailed evolution and interactions are rarely delineated.

[3] When folds grow through lateral propagation and amplitude increases, a space-for-time, e.g., ergodic, substitution can illuminate the long-term spatial and temporal distribution of erosion and surface uplift and can permit reconstruction of progressive changes in the balance between rock uplift and erosion [Burbank *et al.*, 1999]. Ergodic substitutions are most reliable when time constraints exist for several intervals of fold propagation, such that rates of propagation, shortening, rock uplift, and erosion can be determined [Bennett *et al.*, 2006; Sobel *et al.*, 2006]. Such along-strike temporal control, however, is commonly lacking in studies of fold-and-thrust belts. Only when reliable ages can be assigned to various stages of

¹State Key Laboratory of Earthquake Dynamics, Institute of Geology, China Earthquake Administration, Beijing, China.

²Department of Earth Science, University of California, Santa Barbara, California, USA.

³Department of Geology, Appalachian State University, Boone, North Carolina, USA.

⁴Basin and Reservoir Research Center, China University of Petroleum, Beijing, China.

⁵Also at Research Institute of Petroleum Exploration and Development, PetroChina, Beijing, China.

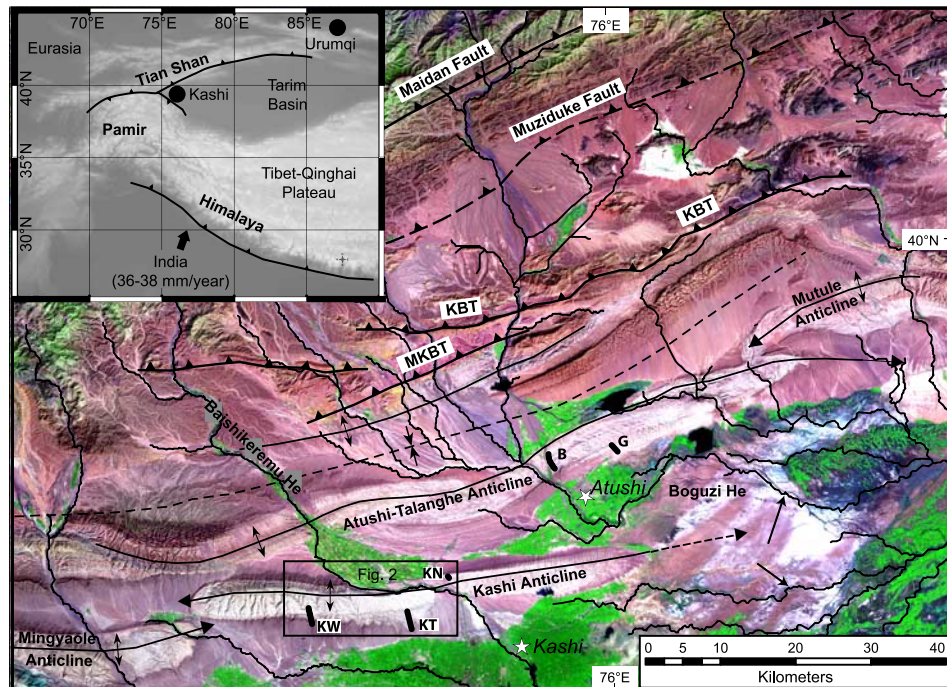


Figure 1. Landsat image of the Kashi basin and southwest Tian Shan. Major thrust faults (thick black lines with teeth on hanging wall) and anticlines are indicated. The South Tian Shan fault system includes the Maidan and Muziduke faults to the north of the Kashi basin. KBT, Kashi Basin Fault; MKBT, Middle Kashi Basin Fault; magnetostratigraphic sections, Boguzihe (B); Ganhangou (G); Kashi West (KW); Kashi Town (KT); and Kashi North (KN), are indicated as thick black bars. Major river drainages generally flow from the NW to SE across the image. Arrows on the east end of the Kashi Anticline indicate that drainage diverge along the projected, but buried crest of the fold. Inset is an elevation map (DEM) of the Tian Shan showing regional setting of the Kashi Basin and location of major range-bounding faults (black lines with teeth on uplifted side). The cities of Urumqi and Kashi are shown by black dots along the flanks of the Tian Shan. DEM varies from <1000 m (dark gray) to >8000 m (white).

fold growth can the validity of the substitution be assessed.

[4] We report here a time-calibrated example of fold propagation from the Chinese Tian Shan, central Asia. We use magnetostratigraphy to directly date the age of growth strata at two sections along the fold. Magnetostratigraphy also allows us to determine local deposition rates that we use to calculate the age of seismically imaged growth strata at a third section along the fold. These data, in combination with the geomorphically expressed and seismically imaged tip of the fold, are used to determine propagation rates and to constrain rates of shortening, surface uplift, and erosion along the fold. We find that present fold shape is strongly influenced by a significant contrast in rock erodability between the outer (younger) conglomerate along the margins of the fold and the inner, weaker fluvial sandstones and shales. In addition, rivers that impinge on the fold margins enhance the topographic asymmetry of the fold. Overall, we show that since the early Pleistocene, the Kashi anticline has propagated eastward at variable rates and that the eastern fifth of the fold remains buried within the aggrading foreland. Once the resistant conglomeratic carapace is breached by erosion, more than 75% of the rock thrust above local base level is subsequently removed. Despite this erosion, the morphology

of the emergent fold mimics spatial variations in the magnitude and rate of shortening and in differential rock uplift.

2. Regional Setting

[5] The Tian Shan represent the most active site of modern intracontinental mountain building in the world, with ~40% of the Indo-Asian convergence being accommodated across this range [Abdrakhmatov *et al.*, 1996; Avouac *et al.*, 1993; Reigber *et al.*, 2001; Wang *et al.*, 2001]. Geodetic results indicate that ~6–9 mm/yr of present-day shortening occurs across the Chinese Tian Shan between the NW Tarim basin and southern Kyrgyzstan [Reigber *et al.*, 2001; Wang *et al.*, 2001]. In contrast to bedrock-cored ranges of the Kyrgyz Tian Shan [Abdrakhmatov *et al.*, 2001; Burbank *et al.*, 1999; Thompson *et al.*, 2002], the style of deformation appears very different in the Chinese Tian Shan on the southern flank of the range (Figure 1), where folds and faults develop within the thick pile of upper Cenozoic strata.

[6] The present topography of the Tian Shan in central Asia was created during Cenozoic times as a result of the India-Asia collision [Allen *et al.*, 1999; Tapponnier and Molnar, 1979; Yin *et al.*, 1998]. The large-scale topographic front of the Tian Shan is delineated by a major south vergent

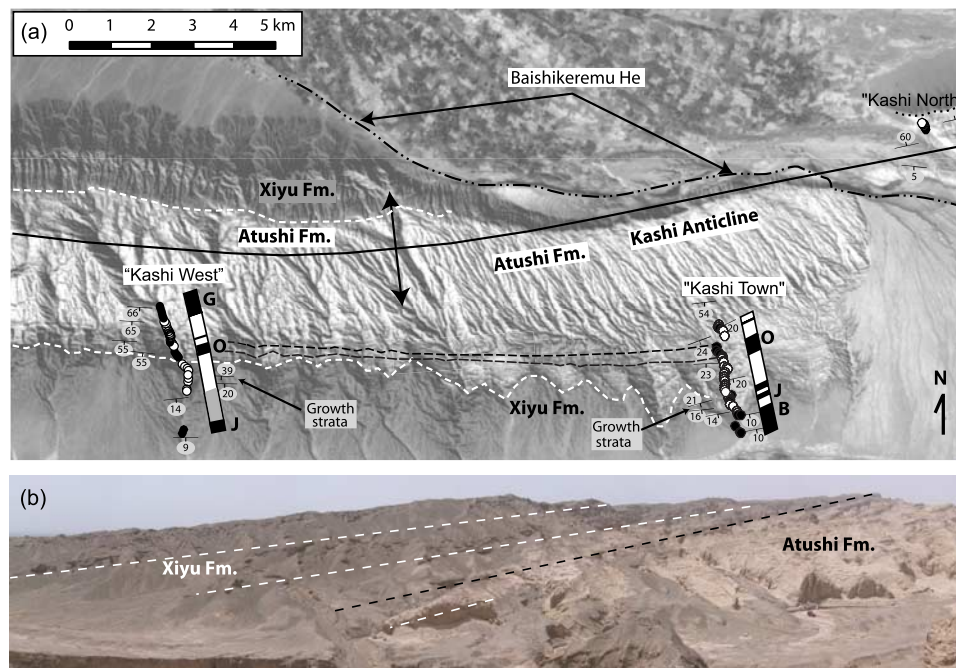


Figure 2. (a) An enlarged CORONA image of the central section of the Kashi fold immediately west of the Baishikeremu He water gap. Three paleomagnetic sampling sections, Kashi West, Kashi Town, and Kashi North are shown. Normal (solid circles) and reversed (open circles) sites are depicted in their appropriate locations, but only some of the sites are shown for clarity. Note that the lower contact of the Xiyu conglomerate (white dashed line) cuts across strike as it interfingers with the Atushi Formation. Kashi West contains 120 sampling sites/levels (E1–E100 collected in 2003, and E144–153, E180–190 collected in 2005). Kashi Town has 52 sampling sites/levels (T0–T52 collected in 2004), Kashi North limb contains eight sites (KN-A to KN-H, 63 samples) sampled in 2003. G, Gauss chron; O, Olduvai subchron; J, Jaramillo subchron; B, Brunhes chron. Black dashed lines depict stratigraphic correlation based on bed tracing between the sections. (b) Photograph of growth strata on the southern limb of the Kashi anticline at the Kashi Town paleomagnetic section. View is to the west. South of a ~700-m-thick panel that dips 20°, offlapping dips of small-pebble conglomerates (darker gray) and sandstone interbeds (light color) are interpreted to record the initiation of folding.

reverse fault system that includes the Maidan and Muziduke faults (Figure 1). These faults represent the Cenozoic reactivation of a late Paleozoic thrust system [Allen *et al.*, 1999; Chen *et al.*, 2000; Xinjiang Bureau of Geology and Mineral Resources, 1993]. Fission track dating by Sobel *et al.* [2006] suggests that exhumation commenced near the Oligocene-Miocene boundary (~24 Ma) along this thrust fault system and that deformation subsequently propagated ~20 km south to the Kashi Basin Thrust (Figure 1), which was exhumed no earlier than 18.9 ± 3.3 Ma.

[7] The Kashi foreland basin is ~160 km long by 70 km wide. As much as 9 km of Cenozoic sediments accumulated in the basin [Jia *et al.*, 2004; Zhou and Chen, 1990] and are folded into a suite of elongate anticlines and synclines (Figure 1) [Li *et al.*, 1996; Scharer *et al.*, 2004]. Palinspastic reconstructions across the basin indicate that >20 km of shortening is accommodated on these major structures [Heermance *et al.*, 2004]. Two areas with contrasting deformational styles are developed in the basin (Figure 1). The northern area represents the westernmost expression of the Kepingtage thrust system as identified by Yin *et al.* [1998]. This area comprises fault-related folds associated with a south vergent imbricated thrust stack (Kashi

Basin Thrust and Middle Kashi basin thrust fault), where slices of Paleozoic strata making up the former Tarim platform are thrust south toward the foreland [Chen *et al.*, 2001; Heermance *et al.*, 2004; Qian *et al.*, 2001; Scharer *et al.*, 2004; Sobel and Dumitru, 1997; Xinjiang Bureau of Geology and Mineral Resources, 1993; Xiao *et al.*, 2000].

[8] Lying south of the Kepingtage system, the Kashi-Atushi fold system represents the southern deformational area. It includes the towns of Kashi (Kashgar) and Atushi (Artush), and is characterized by three sets of en echelon and serial folds [Scharer *et al.*, 2004]. The fold sets vary in length from 80 to 150 km long and have a topographically expressed width of ~10 km. Seismic lines across the folds, however, indicate that the fold flanks are gently dipping in the subsurface and that total anticline width is generally 13–20 km. Five en echelon anticlines, the Mushi (not shown in Figure 1), Mingyaole, Kashi, Atushi-Talanghe, and Mutule (Figure 1), make up three subparallel fold sets that strike east-west from the northeast corner of the external Pamirs to the west end of the Kepingtage thrust belt of the Chinese Tian Shan. Major transverse rivers that drain the Tian Shan cut across the Kashi-Atushi fold system; none are longitudinal.

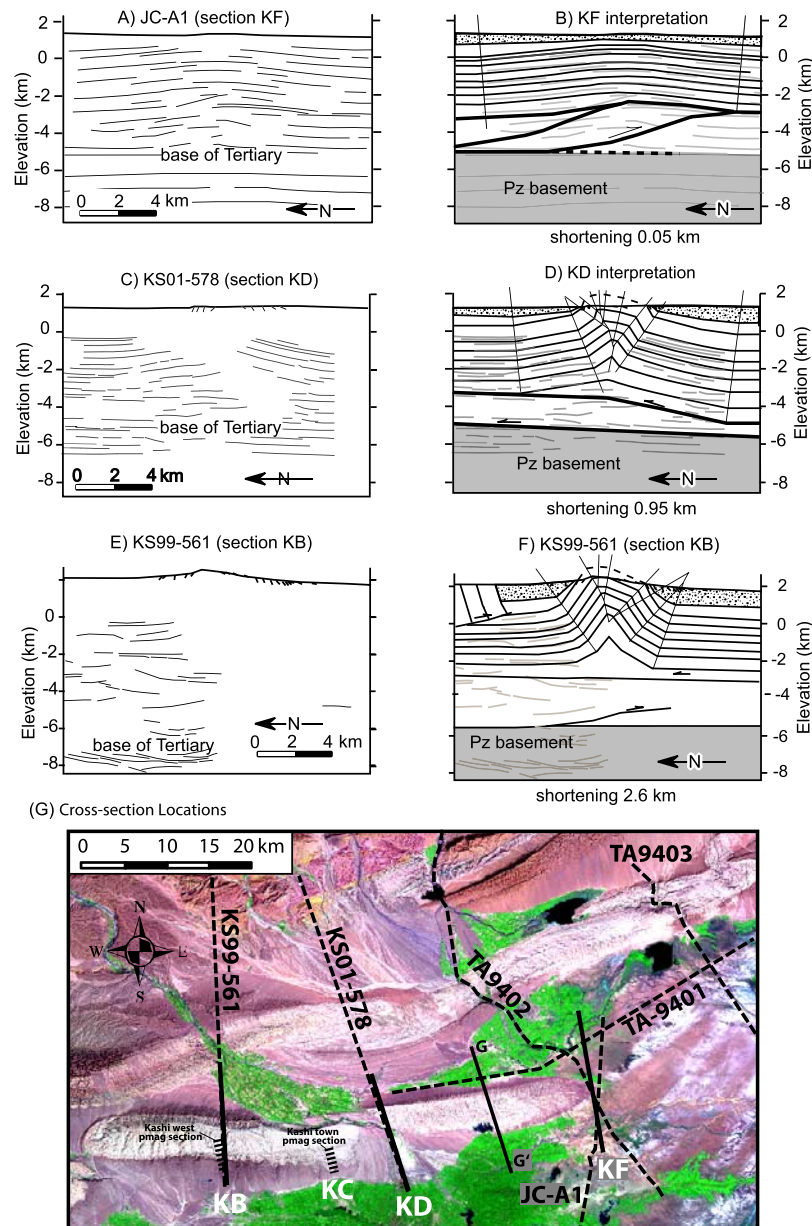


Figure 3. Line drawings from proprietary seismic sections (Figures 3a, 3c, 3e) from PetroChina and corresponding interpreted cross sections for Kashi West (KF), the water gap (KD), and the eastern emergent tip (KB) (Figures 3b, 3d, 3f). Growth strata are drawn as stippled region on the interpreted sections and their thickness is based on the location of fanning dips at the fold flanks at (a, b) section KF or the mapped surface location extrapolated to depth at (c, d) section KD and (e, f) section KB. (g) Landsat image showing the cross sections and seismic line (KS99-561, KS01-578, TA9402, JC-A1, TA9403, TA9410) locations along the Kashi fold. Cross section G-G' is from *Scharer et al.* [2004]. KB and KC are the locations of the magnetostratigraphic sections.

[9] At the surface, the anticlinal structures vary from box-like with ambiguous vergence to asymmetric folds displaying northward vergence [*Scharer et al.*, 2004]. Neogene through Pleistocene strata deposited in the Kashi foredeep crop out in each fold. The outer layers of the anticlines consist of the Xiyu Formation, a moderately well-indurated conglomerate with significant lateral thickness variations (Figure 2). The conglomerate interfingers into a generally fining-down sequence of sandstones, mudstones, siltstones, and gypsum that are well bedded, but weakly indurated

and easily eroded. Even where cross sections indicate that 2–4 km of structural relief has developed, the anticlines are extensively dissected and exhibit ≤ 500 m of topographic relief (Figure 3). Total reconstructed shortening over the last 1–2 Myr across both the Atushi-Talanghe and Kashi folds decreases from ~ 7 to 1 km toward the east [*Chen et al.*, 2002; *Scharer et al.*, 2004]. Overall, these anticlines represent north vergent detachment folds that developed during late Cenozoic times and are interpreted to have accommodated much of the recent shortening that has been shown

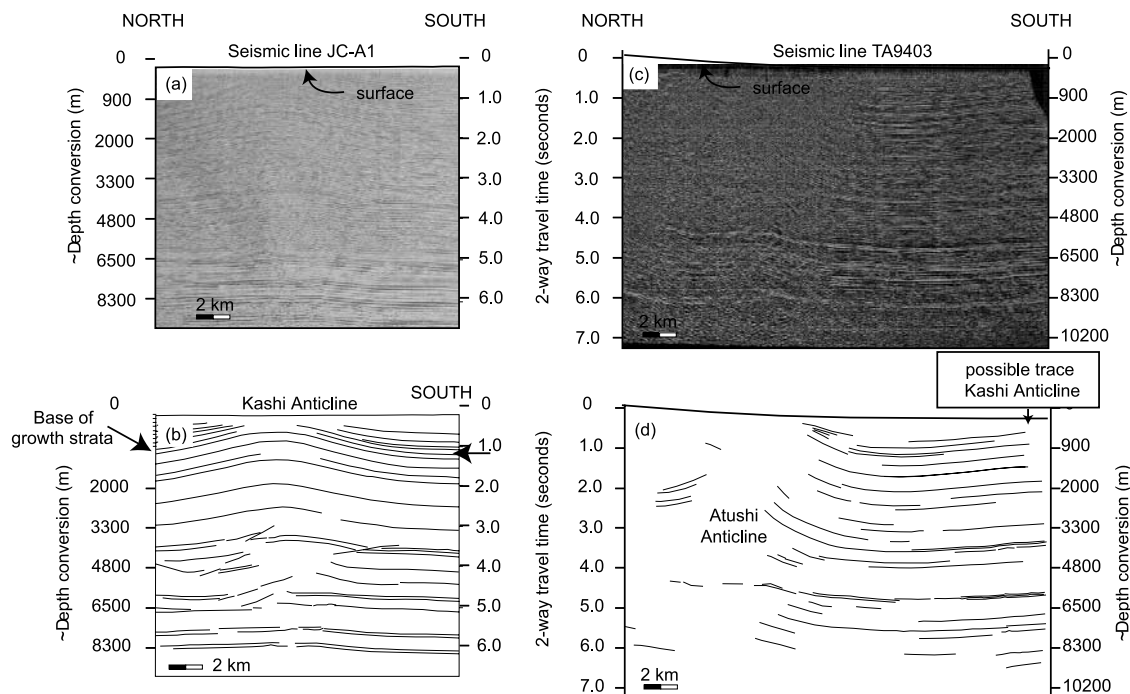


Figure 4. Segments of seismic lines JC-A1 and TA9403 and their line drawing interpretations. All lines are based on two-way traveltimes, and depth conversions are based on the velocity model for the Kashi basin foreland sediments provided by PetroChina. Note that the ground surface is not necessarily at 0 seconds s. (a) Northern part of seismic line JC-A1 (Figure 3g) at the eastern topographic nose of the Kashi Anticline. (b) Line drawing interpretation of JC-A1 showing the Kashi Anticline. Multiple detachment levels and faulting are interpreted between 4000 and 6000 m, but strata above 4000 m behave as a detachment fold. (c) Seismic line TA9403 located ~22 km east of the topographic nose of the Kashi Anticline. (d) Line drawing interpretation of TA9403 showing north dipping beds that may be the northern flank of the Kashi Anticline buried east of the topographic nose.

geotectonically to occur south of the Kyrgyz Tian Shan [Chen *et al.*, 2002; Scharer *et al.*, 2004]. Because these strata have not been deformed by earlier orogenies, they provide a pristine succession within which to discern the style, age, and rates of shortening, as well as ongoing geomorphic modification of the folds.

3. Structure and Stratigraphy of Kashi Anticline

[10] This paper refines the structural interpretation of the Kashi fold presented by Scharer *et al.* [2004] based on additional, improved seismic reflection profiles provided by PetroChina and further structural mapping. The most significant changes are our interpretations of the geometry of faults underlying the fold. Located at the southernmost limit of the Kashi-Atushi fold system, the Kashi anticline is a doubly plunging anticline with an overall north vergence at the surface. The major topographic expression of the fold extends toward N85°E for ~60 km from near the eastern end of the Mingyaole anticline to where its eastern nose plunges into the depositional plain of the Tarim basin (Figure 1). At the surface along its western half, the anticline exhibits steep limbs dominated by dip panels inclined between 50° and 80° (Figures 3d and 3f of Y. Z. Kang *et al.*, Structure feature and an assessment of hydrocarbon potential of the Kashi depression of Tarim basin, Xinjiang unpublished manuscript, 1978, hereinafter referred

to as Kang *et al.*, unpublished manuscript, 1978) separated by relatively flat dips near the axis, which give the fold a box-like shape. Our geologic mapping reveals that reverse faulting occurs locally along the fold flanks, but the faults are neither laterally continuous nor pervasive, and displacements on faults at the surface are much smaller than the displacement at depth required to produce the structural relief on the range itself. Thus folding must be controlled by blind or subhorizontal detachment faults beneath the fold.

[11] Proprietary seismic data from PetroChina reveals that the folds are underlain by at least two detachment levels at ~3 and ~6 km below sea level (bsl), equivalent to 4.5–7.5 km depth (Figures 3 and 4). Low-angle faults are common beneath the folds between these detachment levels, and do not appear to cut strata above depths of ~4.5 km. Despite changing fault dips, the higher structural levels of the folds have a consistent north vergence and steep limbs (>60°, Figures 3d and 3f) that are not parallel to the underlying fault ramps. Where ramps occur below the upper detachment, the strata appear discontinuous (faulted) across the ramp. These geometries suggest that folding of the older Tertiary strata is due to fault bend folding [Suppe, 1983] with limited slip on the faults. Above the upper detachment, the strata typically are not parallel to the underlying fault ramps, the amplitude of folding increases upsection in places, and tight folds occur in the absence of faults. These characteristics suggest detachment folding dominates the

deformation. Duplex structures between -3 and -6 km elevation and flexural slip within the more competent layers above -3 km depth complicate fold kinematics and suggest that the overlying layers likely behave as faulted detachment folds with moderate strain (similar to Figure 3c of Mitra [2002]) or detachment folds above a fault bend fold in the basal layer (analogous to Figure 13d of Gonzalez-Mieres and Suppe [2006]). We therefore interpret these structures as detachment folds above the upper detachment, with strain accommodated below the upper detachment by both faulting and layer-parallel shear. The crest of the Kashi fold forms a broad, gently plunging ($\sim 1.8^\circ$) nose at its eastern end, but an abrupt, steeply plunging anticlinal hinge at its western end, where it interferes with two active folds as it is squeezed between the Mingyaole and Atushi-Talange anticlines (Figure 1).

[12] The Kashi anticline is underlain by three Tertiary sedimentary sequences that unconformably overlie Cretaceous and/or Paleozoic strata: the Miocene Wuqia group, the Plio-Pleistocene Atushi Formation, and the Xiyu Formation, which is traditionally assigned to the Pleistocene [Jia *et al.*, 2004; Kang *et al.*, unpublished manuscript, 1978]. Although not exposed at the surface here, the Wuqia Group in the Kashi Basin (~ 2500 – 4000 m thick) consists of predominantly fine textured, multicolored, interbedded mudstone, siltstone, and fine sandstone, and it includes numerous gypsum interbeds in its lower part [Jia *et al.*, 2004; Zhou and Chen, 1990; R. V. Heermance *et al.*, Tectonic control on gravel progradation and the significance of upward coarsening stratigraphy in the evolving southwestern Chinese Tian Shan foreland, submitted to *Basin Research*, 2006, hereinafter referred to as Heermance *et al.*, submitted manuscript, 2006]. It represents a fluvial-lacustrine sequence with abundant fossils, including ostracoda, charophyte, and foraminifera, that indicate a Miocene age [Hu, 1982; Jia *et al.*, 2004; Zhou and Chen, 1990]. The gypsiferous beds at the base of the Wuqia Group and at ~ -3 km elevation are likely detachment horizons that correspond with the seismically interpreted detachment levels (Figure 3).

[13] Conformably above the Wuqia Group, the Atushi Formation (1500–3400 m thick) is dominated by fluvial, yellow-gray to tan mudstone, siltstone, and fine- to medium-grained sandstone that generally coarsens both upward and toward the west [Jia *et al.*, 2004; Kang *et al.*, unpublished manuscript, 1978]. Thin beds, 5 to 50 mm thick, of gypsum and gypsiferous mudstone are preserved within the lower units and also increase in abundance westward (Kang *et al.*, unpublished manuscript, 1978), whereas at stratigraphically higher levels, pebble conglomerate layers are sparsely interbedded. The age of the Atushi Formation is given as Pliocene, based on magnetostratigraphic data [Chen *et al.*, 2002] and the presence of ostracoda in the Boguzihe section [Jia *et al.*, 2004]. Paleocurrent directions in the upper part of this sequence at the Kashi West and Boguzihe paleomagnetic sections are oriented predominantly eastward (Heermance *et al.*, submitted manuscript, 2006) and indicate a major change in the drainage network since the Plio-Pleistocene.

[14] The top of the Atushi Formation is marked by an abrupt coarsening and darkening of the lithology that is easily mapped in the study area and indicates transition into

the Xiyu Formation (Figure 2). The Xiyu Formation is dominated by massive, thickly bedded, pebble-to-cobble conglomerate typical of the channel and debris flow deposits of alluvial fans and gravel bedded braided rivers, locally interbedded with minor lenticular sandstone and mudstone beds in its lower part. The Xiyu and Atushi Formations appear conformable, but the stratigraphic level of the contact is highly variable along strike and becomes relatively younger eastward (Kang *et al.*, unpublished manuscript, 1978). The lateral discontinuity of the Xiyu Formation can be seen northwest of the city of Kashi in the Landsat imagery (Figure 2a), where the dark Xiyu conglomerate pinches out into the lighter Atushi sediments to the east. The stratigraphic height of the Atushi-Xiyu contact also appears to vary in a north-south direction. This variation is expressed stratigraphically by the distance between the axial trace of the fold and the position of the Xiyu Formation on the fold's north versus south flanks (Figures 1 and 2a). Despite the essentially identical geometry of the fold limbs and an absence of major thrust faults, the Atushi-Xiyu contact on the north side of the anticline is consistently and significantly closer to the hinge line than is the contact on the south side [Scharer *et al.*, 2004; Kang *et al.*, unpublished manuscript, 1978]. We interpret this contact to be progradational and relatively younger on the southern limb and eastern part than on the northern limb and western part of the anticline [Scharer *et al.*, 2004]. Paleomagnetic results in the Kashi basin show that the conglomeratic Xiyu Formation is clearly time-transgressive along its progradational contact with the underlying Atushi Formation, such that the onset of conglomeratic deposition varies by ~ 1 Myr across a distance of 10 km [Chen *et al.*, 2002; Heermance *et al.*, 2004].

[15] Beneath and along the flanks of the Kashi fold (Figure 3), beds of the Wuqia Group and in the lower part of the Atushi Formation are seismically constrained to be parallel and to display approximately constant stratigraphic thickness [Qian *et al.*, 2001]. Overall, folding of these beds defines the structural geometry of the Kashi anticline, and we interpret them as pregrowth strata. In contrast, beds of the upper Atushi Formation to Xiyu Formation are arranged in a fan-like pattern around the outer flank of the anticline, and they thin as they approach the anticline crest (i.e., Figures 2b and 3a–3f). Syntectonic intraformational unconformities [Riba, 1976] are common in these beds, and we interpret them as growth strata.

4. Magnetostratigraphy and Rate of Sedimentation

4.1. Paleomagnetic Sampling, Laboratory Methods, Statistical Analysis, and Results

[16] In order to define the timing of fold growth and its stratigraphic context, we established magnetic polarity stratigraphies of the associated sediment succession at two measured sections along the southern limb of the anticline: Kashi West (KB) and Kashi Town (KC), separated by ~ 13 km (Figure 2a). Within the framework of the local Plio-Pleistocene fossil assemblage, the resulting succession of reversals was then correlated to the geomagnetic polarity timescale (GPTS) of Cande and Kent [1995] (Figure 5). The stratigraphy of the sections was linked together by tracing bedding along intervening strata. This correlation was

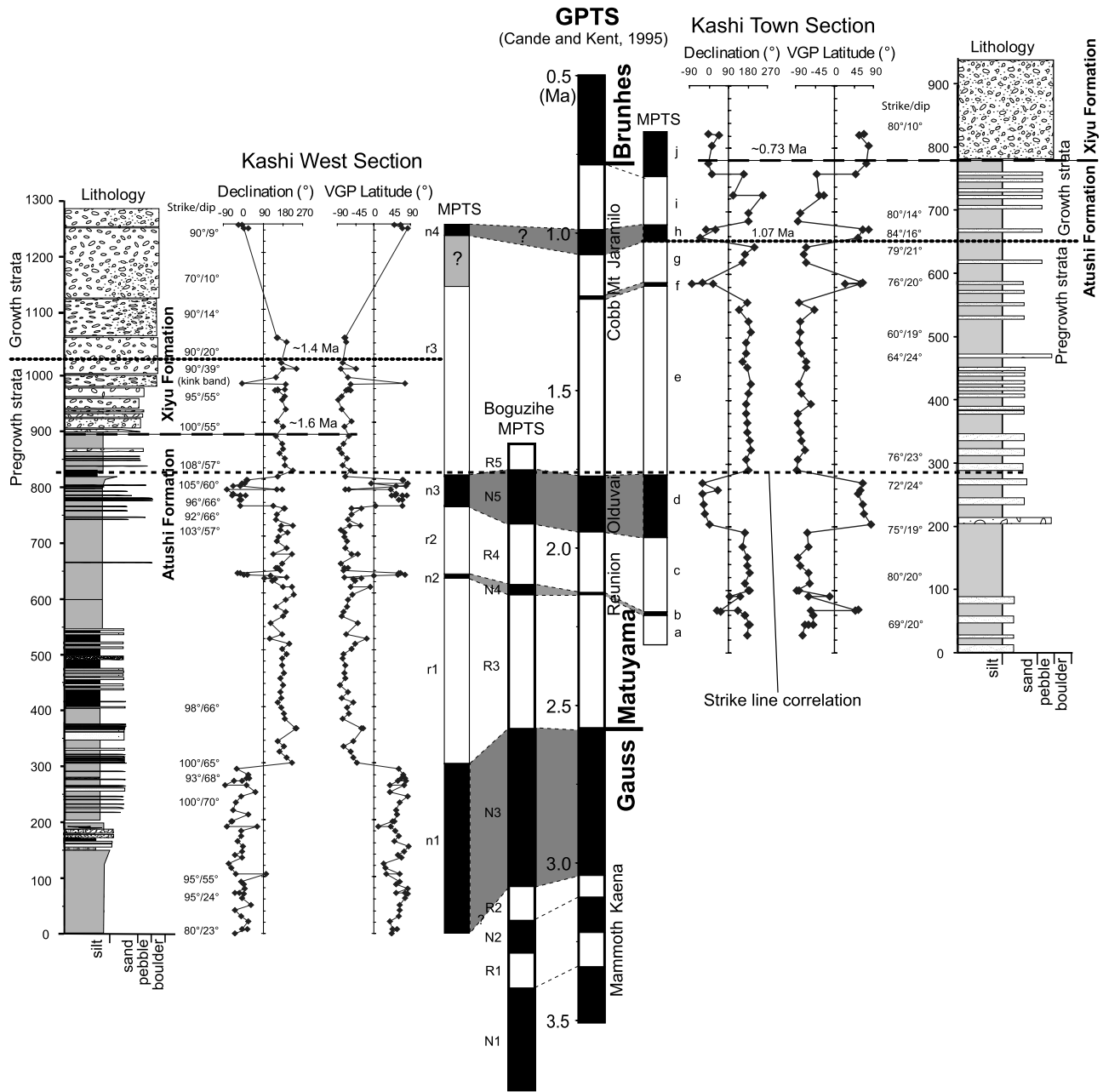


Figure 5. Lithology and magnetostratigraphic results from the Kashi West and Kashi Town sections with declination and virtual geomagnetic pole (VGP) plotted against stratigraphic height and correlation to the GPTS of *Cande and Kent* [1995]. The polarity record of the Boguzihe section in the Atushi-Talange anticline to the north [*Chen et al.*, 2002] is shown. Strike line mapping correlates the two sections at ~830 m (Kashi West) and ~285 m (Kashi Town). Given the Plio-Pleistocene age of these strata, only the correlation of the youngest normal polarity zone (n4) at Kashi West is ambiguous, due to the 200-m gap in sampling through the Xiyu conglomerate.

subsequently tested by matching the observed reversals within the stratigraphic sequences between the two sections (Figure 2a).

4.1.1. Sampling

[17] The paleomagnetic sampling for the Kashi West section begins in the upper Atushi Formation and ends in the lower Xiyu Formation, above which coarse-grained facies prohibited further sampling (Figure 5). Strike line mapping demonstrates that the upper Atushi succession of

the Kashi Town section is stratigraphically equivalent to the Xiyu Formation at the Kashi West section (Figure 2a). At the Kashi Town section, finer-grained sediments allow us to sample across the syntectonic unconformity and to define the initial age of the growth strata more precisely.

[18] Stratigraphic thicknesses were measured with either tape-and-compass survey or Jacob staff and Abney level. At least two to three oriented cores were drilled at each of 120 sedimentary horizons in the 1250-m-thick Kashi West

section using standard techniques with gasoline-powered drills and 2.5-cm-diameter diamond coring bits. Cores were oriented in situ with a magnetic compass and, where possible, by sun compass [Butler, 1992]. Sites were spaced 2–10 m apart stratigraphically. Similarly, two to three oriented cores were drilled at each of 52 sites in the 800-m-thick Kashi Town section, with sample spacings of 0.5–30 m. Variation in site spacing was necessary so as to obtain suitably fine-grained lithologies and to avoid disturbed or highly altered sediments. Sampling to the top of either section was not possible due to the massive conglomerates of the Xiyu Formation and the scarcity of suitable lithologies.

[19] In order to perform a significant fold test, 63 samples at eight sites were collected on the northern limb of the Kashi anticline along the Baishikeremu He (Figure 2a). These eight sites are in pregrowth strata and stratigraphically correlate to the lower part of the Kashi West paleomagnetic section.

4.1.2. Measurements

[20] The Kashi West section and the northern limb of the Kashi anticline yielded 163 specimens that were measured using a fully automated 2G Enterprises 755 SRM DC-SQUID cryogenic long-core magnetometer with a background noise level of ~ 300 – 400 pA m² at the Laboratory for Paleo- and Rock Magnetism, GeoForschungsZentrum Potsdam. Another 98 specimens from the Kashi Town and Kashi West sections were analyzed at the California Institute of Technology paleomagnetism laboratory, using a three-axis DCSQUID moment magnetometer system housed in a magnetically shielded μ -metal room. The background noise of this instrument is <1 pA m², and it is equipped with a vacuum pick-and-put, computer-controlled sample handling system which can measure up to 180 samples automatically [Ward et al., 2005]. AF demagnetization was performed with a computer-controlled, three-axis coil system. Thermal demagnetization was performed in a commercially built, magnetically shielded furnace.

[21] One specimen per sampling site/level was initially measured for natural remnant magnetization, and then subjected to low alternating field (AF) demagnetization up to 10 mT at ~ 2 mT steps to remove low-coercivity magnetizations. The specimens were then treated with stepwise thermal demagnetization using at least 9 to 12 demagnetization steps typically in (1) 150°C steps up to 300°C, (2) 100° or 50° steps up to 500°C or 550°C, and (3) 40° or 30° or 20° steps up to 680° or 690°C. At each site, a second and third specimen was demagnetized if the first yielded unstable or overprinted directions or if an interval of normal or reversed polarity was defined by only one specimen.

4.1.3. Paleomagnetic Results

[22] The intensity of the natural remnant magnetism (NRM) for these specimens was of the order of 10^{-2} – 10^{-3} A/m. Progressive demagnetization successfully resolved multiple components of magnetization. Equal area projection and orthogonal vector plots reveal two clear components for the vast majority of the specimens: a high-temperature component (HTC) and a low-temperature component (LTC) (Figure 6). The LTC, which is a low-coercivity, low-blocking temperature component, is removed by AF demagnetization at 30 or 60 gauss and thermal demagnetization at 150°C or 300°C. Typically, the

LTC does not decay toward the origin. The HTC is normally completely unblocked at temperatures of 580°C, and the magnetization commonly becomes unstable above 580°C (Figure 6), which is characteristic of magnetite. The vast majority of the specimens possess this type of demagnetization. However, in some specimens (as seen elsewhere in the Tian Shan foreland [Charreau et al., 2005]), 15% or more of the original NRM intensity remains after 580°C, and this magnetization persists until 670°C or 680°C (Figure 6): a behavior characteristic of hematite. When both magnetite and hematite were present in the same specimen (Figure 6, E185.1), no significant difference in remanent direction was observed when comparing the 400°–580° or 590°C with the 610–690°C parts of the unblocking spectra. This suggests that both magnetic carriers recorded the same paleomagnetic field when their remanences became fixed in the rock.

[23] To determine characteristic remanence (ChRM) directions, principal component analysis [Kirschvink, 1980] was performed for each specimen using paleomagnetic software of Jones [2002] and N. R. Nowaczyk (personal communication, 2004). Data from a minimum of four, and more typically five to eight, temperature steps were used for least squares fits, in which the origin of the vector component diagram was included as an additional datum. Typical maximum angular deviation was between 1° and 6°. Magnetic characteristics were found to be laboratory-independent. Because of unstable HTC, in the Kashi West section, 19 out of 158 specimens yielded ambiguous polarity and were rejected, whereas in the Kashi Town section, 11 out of 70 specimens yielded ambiguous results and were rejected.

[24] Only demagnetization lines with maximum angular deviation values $<10^\circ$ were included in the statistical analysis. Mean directions were obtained using Fisher statistics. Tilt corrections improve the grouping of ChRM inclinations significantly when both sections are considered together (Figure 7). Because both sections display generally steep homoclinal dips, the grouping of site-mean ChRM declinations within individual sections is only slightly improved by tilt corrections.

[25] The reversal test followed that of McFadden and McElhinny [1990]. Although the directions from both Kashi West and Kashi Town sections pass the reversal test with a “C” classification (Figures 7a and 7b), we note a significant difference in inclination values, such that the mean reversed polarity inclinations in both sections are 8°–9° less steep than those of normal polarity. This difference is most likely due to an unremoved overprint [Charreau et al., 2005; Gilder et al., 2001; McElhinny, 1964; Quidelleur and Courtillot, 1996] that because of the folding geometry and the present magnetic field direction, steepens the normal polarity directions and causes the reversed polarity directions to be gentler.

[26] The eight sites sampled on the north limb of the Kashi anticline yielded similar demagnetization characteristics as those from the Kashi West and Kashi Town sections and possess both normal and reverse polarities (sites KN-A-H in Table 1). These data pass the reversal test with a “B” classification (Figure 7c). In order to perform a meaningful fold test, we grouped the Kashi West and Kashi Town magnetostratigraphic sections into three mean normal

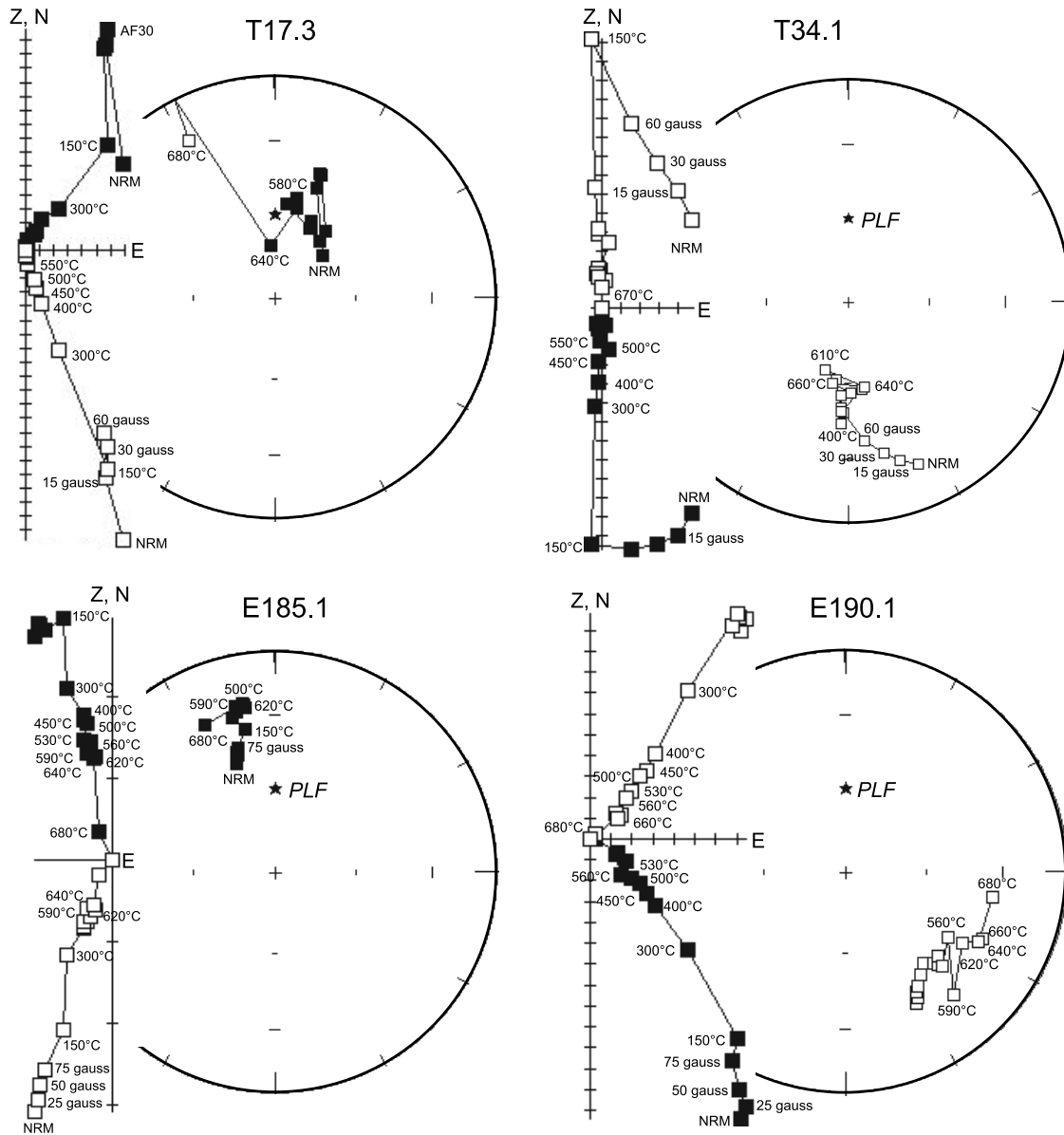


Figure 6. Representative data (Zijderveld diagrams and equal-area projections) during alternating field and thermal demagnetization in tilt-corrected coordinates. The reversed characteristic remanence direction can easily be distinguished from a present-day overprint due to the steep bedding dips in this study. Each division in the Zijderveld plots equals 10^{-5} emu; open (solid) squares represent inclination (declination); solid squares and present local field (PLF, star) represent lower hemisphere projections in the equal-area plots. Sample T17.3 reveals a characteristic remanence direction between $\sim 150^{\circ}\text{C}$ and 580°C . Erratic directions at high temperatures indicate magnetite as the primary remanence carrier. For samples T34.1 and E190.1, 90% of the magnetic intensity is lost by 580°C , but consistent directions are found at higher temperatures, suggesting both magnetite and hematite are present. Sample E185.1 behaves similarly but has lost only 65% of its intensity by 580°C , suggesting a stronger contribution from hematite.

directions and four mean reversed directions, respectively (Table 1), and combined these groups with the data from the northern fold limb. Stereonet plots of the 15 site mean directions before and after tilt corrections (Figure 7d) display a significant increase in clustering of the directions after tilt corrections with $\kappa_s/\kappa_g = 25.5$ ($D_g = 19.2$, $I_g = 70.8$, $\kappa_g = 1.89$ and $\alpha_{95g} = 48.22$ before tilt correction and $D_s = 354.0$, $I_s = 52.9$, $\kappa_s = 48.22$ and $\alpha_{95s} = 5.37$ after tilt

correction). These data pass the fold test at the 99% confidence level [McElhinny, 1964]. The combination of the positive results from the fold and reversal tests, as well as the presence of layer-bound magnetic polarity zones, strongly imply that these ChRM directions were acquired by the sediments at or soon after deposition. The expected paleomagnetic pole position for the Plio-Pleistocene at the studied area is essentially the same as the current pole

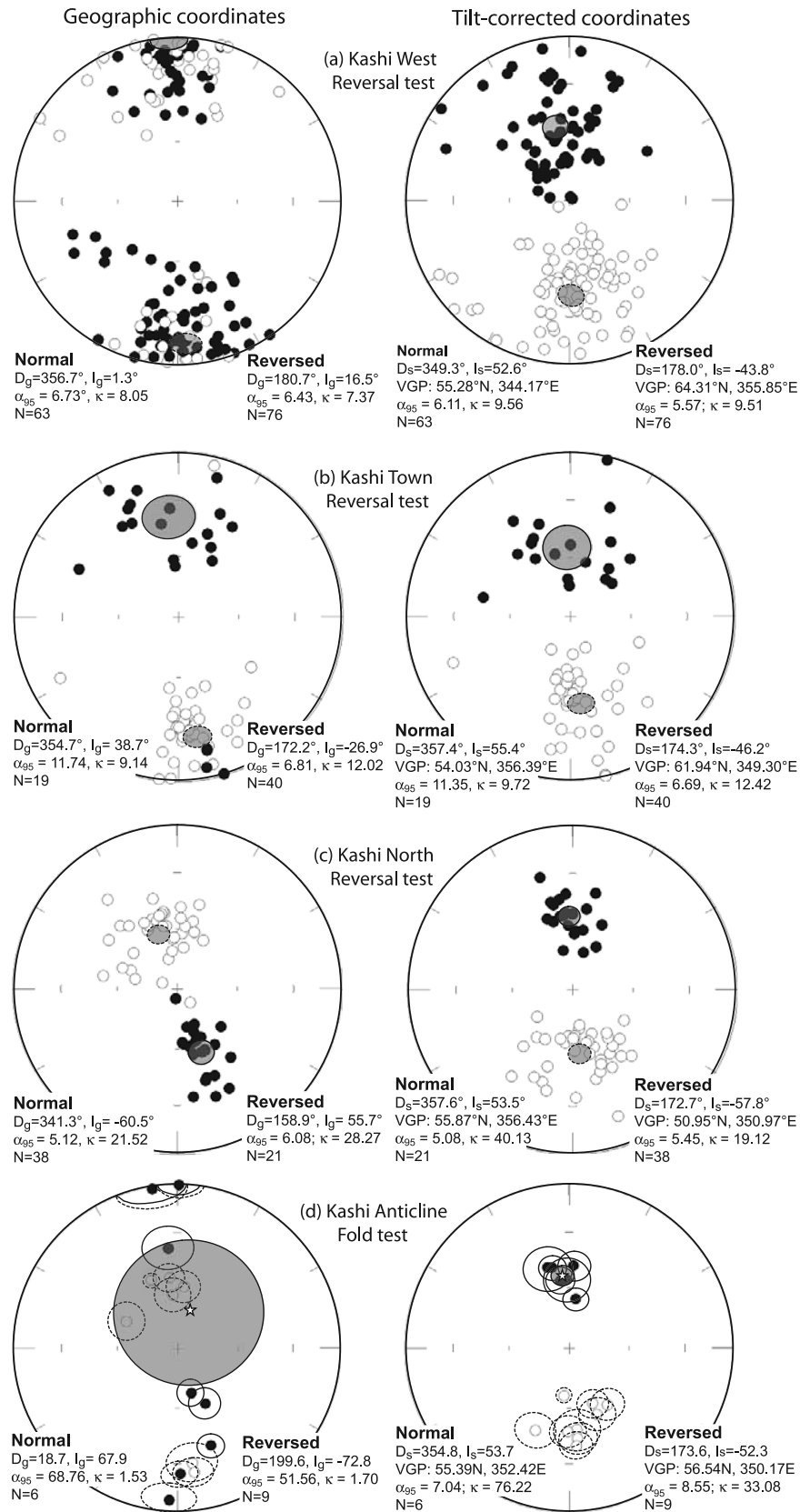


Figure 7. (a, b, c) Reversal tests of paleomagnetic stability in the Kashi West, Kashi Town, and Kashi north limb sections, respectively. (d) Fold test of paleomagnetic stability. Gray (shaded) circles represent the mean directions in both polarities. Open stars in Figure 7d represent overall mean normal directions in both polarities.

Table 1. Site-Mean Paleomagnetic Directions Used for Fold Test^a

Site	Bedding		n	D _g , deg	I _g , deg	D _s , deg	I _s , deg	κ _g	α ₉₅ , deg	κ _s	α _{95s} , deg
	Strike	Dip									
KW-A	70–100°	20–66°	39	178.5	24.1	175.7	−40.0	10.73	7.34	10.69	7.34
KW-B	70–100°	20–66°	37	183.1	7.8	180.8	−47.9	6.09	10.43	8.71	8.47
KW-C	70–100°	20–66°	27	351.1	1.8	345.0	47.9	5.71	12.79	6.88	11.45
KW-D	70–100°	20–66°	35	0.6	0.2	352.6	55.6	11.91	7.33	13.51	6.85
KT-A	70–84°	10–20°	19	354.7	38.7	357.4	55.4	9.14	11.74	9.72	11.35
KT-B	70–84°	10–20°	20	172.4	−29.8	174.5	−48.7	9.62	11.10	10.14	10.78
KT-C	70–84°	10–20°	20	172.2	−24.3	174.6	−44.0	15.56	8.55	15.57	8.54
KN-A	255°	62°	7	5.7	−59.1	146.2	−55.7	46.97	8.23	47.02	8.22
KN-B	255°	62°	6	355.1	−63.4	157.3	−54	50.07	8.71	50.03	8.72
KN-C	260°	59°	8	298.1	−61.3	202.2	−44.9	31.20	9.40	31.18	9.41
KN-D	260°	59°	8	339	−53.5	186.2	−66.1	184.54	3.82	184.05	3.83
KN-E	256°	65°	7	353.6	−54.4	157.1	−60	57.17	7.44	57.14	7.45
KN-F	256°	65°	8	162.7	66.6	348.0	48.4	62.62	6.59	62.68	6.59
KN-G	260°	71°	7	153.1	58.8	3.1	48.3	54.23	7.65	54.24	7.65
KN-H	260°	75°	6	160.9	37.3	7.6	65.3	99.53	6.16	100.00	6.14
Average			15	19.2	70.8	354.0	52.9	1.89	36.79	48.22	5.37

^aSubsections KW-A to KW-D, magnetostratigraphic sections Kashi West (KW); subsections KT-A to KT-C, Kashi Town (KT); sites KN-A to KN-H, northern limb of the Kashi anticline at the water gap, respectively. Abbreviations are n, number of specimens or sites; D, magnetic declination; I, magnetic inclination; g, geographic coordinates; s, stratigraphic coordinates; κ, precision parameter; α₉₅, radius of the cone in which the mean direction lies within 95% confidence.

position: declination 360.0°, inclination 58.8° for site latitude 39.56°N. The overall mean direction of tilt-corrected site-mean ChRM directions for 15 sites from the Kashi West, Kashi Town sections, and Kashi north limb is shown in Table 1 (n = 15). Using the methods of *Demarest* [1983], a comparison of the expected and observed directions yields flattening of inclination, $F \pm \Delta F = 5.9 \pm 6.1^\circ$, and no significant vertical axis rotation and error $R \pm \Delta R$ of $-6.0 \pm 8.7^\circ$ (negative sign indicates counterclockwise).

4.2. Magnetostratigraphy and Correlation to the Geomagnetic Polarity Timescale

[27] Virtual geomagnetic pole latitudes and declinations for individual specimens were plotted against stratigraphic height for each of the Kashi West and Kashi Town sections, resulting in a magnetic polarity sequence for the upper parts of the Atushi Formation and Xiyu Formation. The resultant magnetostratigraphy (Figure 5) reveals four periods of normal polarity (n1 through n4) and three periods of reversed polarity (r1 through r3) in the Kashi West section, and five periods of reversed polarity (a, c, e, g, i) and five periods of normal polarity (b, d, f, h, j) in the Kashi Town section, respectively. All intervals are represented by at least two sites from different strata levels, except two intervals (b and f in the Kashi Town section, Figure 5) which lie within a single sedimentary layer. For these two intervals, the polarity was confirmed by demagnetizing a second or third specimen that was drilled 5–40 cm from the initial specimen. A short normal chron at ~1000 m in chron r3 was omitted because only one specimen was collected during the 2003 field season from this site in a small lens of silty fine sand interbedded within the massive conglomerates. This specimen was measured in the GFZ lab in 2003. In order to check the robustness of this normal chron, we revisited this site in 2005. Unfortunately, we could not find any suitable lithology for sampling, and only found one silt lens about 2 m and 10 m below, and 10 m above this site, respectively. We collected four more samples and analyzed them in California Institute of Technology lab in 2006. All these data show unambiguous reversed polarity, and we

therefore do not include the single-specimen normal-polarity sample in our magnetostratigraphy.

[28] The age spanned by the sampled stratigraphic units is generally considered to be $\ll 10$ Ma, a claim based on regional lithostratigraphic correlation which is supported by biostratigraphic and magnetostratigraphic control [*Chen et al.*, 2002; *Jia et al.*, 2004; *Xinjiang Bureau of Geology and Mineral Resources*, 1993; *Zhou and Chen*, 1990]. In the nearby Boguzihe and Ganhangou sections, a convincing correlation of the upper Atushi and lower Xiyu strata can be made to the GPTS and indicates they span an interval from ~3.5 Ma (base of the Gauss chron) to ~1.0 Ma (Jaramillo subchron) [*Chen et al.*, 2002]. Given the fact that the Xiyu conglomerate has generally prograded southward [*Chen et al.*, 2002; *Heermance et al.*, submitted manuscript, 2006], we expect the Kashi sections to span a similar, but slightly younger time interval. Strike line mapping between the Kashi West and Kashi Town sections matches polarity zones between them and enables us to define an extensive interval of dominantly reversed magnetization that we assign to the Matuyama chron (Figure 2). No significant unconformities were identified within the sampled sections. Given the fine-grained deposition through much of each section, we expect steady accumulation of sediments during which large rate changes are absent.

[29] We used the following criteria to correlate the Kashi West and Kashi Town magnetostratigraphy to each other, to the Boguzihe magnetostratigraphy in the Atushi-Talange anticline [*Chen et al.*, 2002, Figure 5], and to the GPTS of *Cande and Kent* [1995]: (1) The upper part of the Boguzihe section encompasses the upper Atushi Formation and the base of the Xiyu conglomerate and spans a similar pattern of reversals, including the dominantly reversed interval of the Matuyama chron, (2) outcrop strike line tracing between the Kashi West and Kashi Town sections affirms the magnetic correlations between them and the younger age of the upper section at Kashi Town (Figures 2a and 5), (3) the dominantly normal and reversed polarities of the Gauss and Matuyama chrons, respectively, are distinctive and well

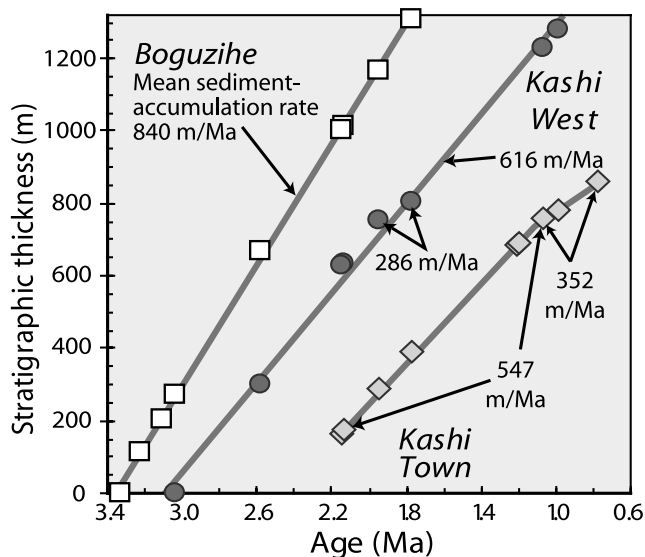


Figure 8. Sediment accumulation plot of the Kashi West, Kashi Town, and Boguzihe sections using data and correlations from Figure 5. The slope of the lines is equivalent to the mean sediment accumulation rate (not corrected for compaction) for each section. Whereas rates are fairly constant in the Boguzihe and Kashi West sections, rates apparently slow at ~ 1.0 Ma in the Kashi Town section. This deceleration is consistent with the appearance of growth strata indicating the initiation of differential uplift at this time.

expressed in our magnetic data from Kashi, (4) the regional stratigraphic correlation of Atushi Formation and Xiyu conglomerates between the Kashi anticline and Atushi-Talanghe anticline (Figure 1) [Scharer *et al.*, 2004], (5) the measured sediment accumulation rate of ~ 840 m/Myr in the Boguzihe paleomagnetic section ~ 27 km to the NE in the Atushi-Talanghe anticline is similar to the interpreted rates of sedimentation from the Kashi anticline (Figures 1 and 8), (6) the absence of significant hiatuses or faults throughout the section, and (7) the probability that both sections lie within the Pliocene-Quaternary [Chen *et al.*, 2002; Jia *et al.*, 2004; Xinjiang Bureau of Geology and Mineral Resources, 1993; Zhou and Chen, 1990]. With these constraints, we find a convincing match of the Kashi Town section with the GPTS between Brunhes chron and Reunion subchron. Our preferred correlation (Figure 5) represents the best available fit in terms of interval number and duration. With respect to the GPTS, problems in correlation lie between subchrons n3–n4 in the Kashi West section due to insufficient sampling into massive conglomerates, where normal event n4 could be correlated to the Cobb Mt., Jaramillo subchron or Brunhes chron. We prefer to correlate it to Jaramillo subchron to remain consistent with the mean accumulation rate of 500–600 m/Myr (Figure 8) and outcrop strike line correlation to the Kashi Town section (Figures 2 and 5).

4.3. Rate of Sediment Accumulation and Age of Growth Strata

[30] Given these correlations to the GPTS, comparing stratigraphic thickness with magnetostratigraphic ages reveals a linear trend in sediment accumulation rates

through time for the Boguzihe and Kashi West sections and for the lower part of Kashi Town section (Figure 8). The mean accumulation rate of the Kashi Town section, however, decreased from ~ 550 m/Myr in its lower part to ~ 350 m/Myr in the upper section around ~ 1 Ma, which coincides with the initial deposition of growth strata. We also note that mean sediment accumulation rate may decrease to ~ 290 m/Myr during the Olduvai subchron in the Kashi West section. On the basis of magnetic correlations and extrapolated accumulation rates, the base of the Xiyu Formation ranges from ~ 0.7 Ma in the Kashi Town section to ~ 1.6 Ma in the Kashi West section ~ 13 km to the west (Figure 5). At the Kashi Town section, the growth strata occur higher in the stratigraphic section than in the Kashi West section (Figures 2a and 5). Within the Jaramillo subchron, growth strata indicate folding at 1.07 ± 0.03 Ma in the Kashi Town section. In the context of the magnetic correlations and based on rates extrapolated above the top of the Olduvai subchron, folding of the Kashi anticline initiated at $1.4_{-0.2}^{+0.17}$ Ma in the Kashi West section. Errors associated with growth strata result from the need to interpolate between reversal boundaries of known ages, the uncertainty in the stratigraphic position of the base of the overlying normal magnetozone, and small uncertainties on the precise location of the growth strata within the magnetic section (Figure 5).

[31] Seismic line JC-A1 across the eastern topographic tip of the Kashi fold shows fanning dips and beds that off-lap the fold flanks (Figures 4a and 4b). We interpret these as growth strata [Riba, 1976]. By carefully mapping the depth on the seismic line of the lowest strata that off-lap the fold, we define a depth of 0.5 ± 0.1 km below the surface (Figures 4a and 4b) for growth strata in the undeformed basin. On the basis of the deposition rates of 547–840 m/Myr from the Kashi Town section ~ 32 km east and the Boguzihe section ~ 15 km north [Chen *et al.*, 2002], an age of 0.8 ± 0.3 Ma is calculated for the oldest growth strata (Table 2). The large error on our age estimation is due to the 20% uncertainty in the exact depth of the growth strata and the difference in sediment–accumulation rates between Kashi Town and Boguzihe. We use the deposition rates from pregrowth strata to estimate growth strata ages because we base our calculation on stratigraphic depths within the undeformed basin, where rates should remain relatively constant in contrast to rates above the active fold, where a decrease in deposition rates is observed.

5. Growth, Lateral Propagation, and Rates

5.1. Structural Cross Sections and Shortening

[32] Three cross sections were constructed from structural measurements [this study; Scharer *et al.*, 2006] and observations in the seismic sections (Figures 3 and 4). Dip domains are typically separated by kink hinges, as observed in the field and based on the mapping of Kang *et al.* (unpublished manuscript, 1978). Short sections of moderately to gently dipping beds on the fold crest were included, resulting in rounded folds with minimized shortening. These sections, from west to east are (1) the Kashi West paleomagnetic section (KB), (2) the Baishikeremu He water gap section (KD), and (3) the eastern emergent tip of the fold (KF). Line drawings of proprietary seismic data

Table 2. Summary of Shortening, Shortening Rate, and Vertical Uplift Rate Estimates for Structural Cross Sections

Cross Section	Shortening Method				Average Shortening Rate, km/Myr	Average Vertical Uplift Rate, km/Myr	Initiation of Folding, Ma	Reference
	Line Length		Excess Area					
	Kilometers	Error	Kilometers	Error				
KB (Kashi West)	2.1	0.1	2.6	0.1	$1.7^{+0.5}_{-0.4}$	$1.8^{+0.4}_{-0.3}$	$1.4^{+0.17}_{-0.2}$	this study
KC (Kashi Town)	-	-	-	-	-	1.07 ± 0.03	-	this study
KD (Water gap)	0.09	0.02	0.935	0.145	$0.95^{+0.3}_{-0.2}$	$1.9^{+0.5}_{-0.3}$	$1.0^{+0.08}_{-0.1}$	this study
KF (East end)	0.054	0.055	-0.013	0.087	$0.06^{+0.06}_{-0.03}$	$0.6^{+0.6}_{-0.3}$	0.8 ± 0.3	this study
Kashi East (G-G')	0.2	-	0.7	-	-	-	-	Scharer et al. [2004]

(courtesy of PetroChina) across the Kashi anticline (Figures 3 and 4) constrain fold width and subsurface structure beneath the fold and allow determination of shortening across it.

[33] A very strong reflector, which we infer as the base of the Tertiary section at ~5 km below sea level (bsl) is observed in all the seismic lines (Figures 3 and 4). Our stratigraphic mapping elsewhere within the Kashi foreland has identified at least three potential detachment horizons that correlate to 5 km, 4.5 km, and 2.5 km bsl and lie within gypsiferous horizons, consistent with seismic interpretation of multiple detachment levels between 2.5 and 5 km bsl (Figure 3). Given that the elevation of the Tarim basin floor varies between 1200 and 2000 m along the flanks of the Kashi fold, the likely detachment horizons occur between 3.7 and 7 km depth beneath the fold.

[34] Whereas flat-ramp-flat geometries, as seen here in the lower part of several seismic sections (Figure 9), are typically interpreted as fault bend folds [e.g., Suppe, 1983], bedding geometries and the absence of faults in the upper

part of the three sections are more consistent with detachment folding above the upper detachment at ~2.5 bsl. Our shortening estimates for the detachment folds utilize both line length excess area calculations. *Epard and Groshong [1993]* showed that the excess area data (area below a folded horizon and its previously undeformed level) plotted against the height of each stratigraphic level above the detachment horizon define a line with slope equal to shortening across the fold (Figure 9). As previously discussed, multiple detachment levels are visible in the seismic profiles beneath the Kashi fold. We plot excess area calculations only for those horizons that lie above the upper detachment level, because these strata likely deformed via flexural slip and are unfaulted. We plot the height of each deformed horizon relative to the lowest detachment level (just above the Paleozoic bedrock), usually ~ 5.5 km bsl. Thus the slope of the line through any set of data from an individual fold (Figure 9) is relative to only the unfaulted horizons, is independent of actual detachment depth for that fold, and estimates shortening within the upper 4–5 km of

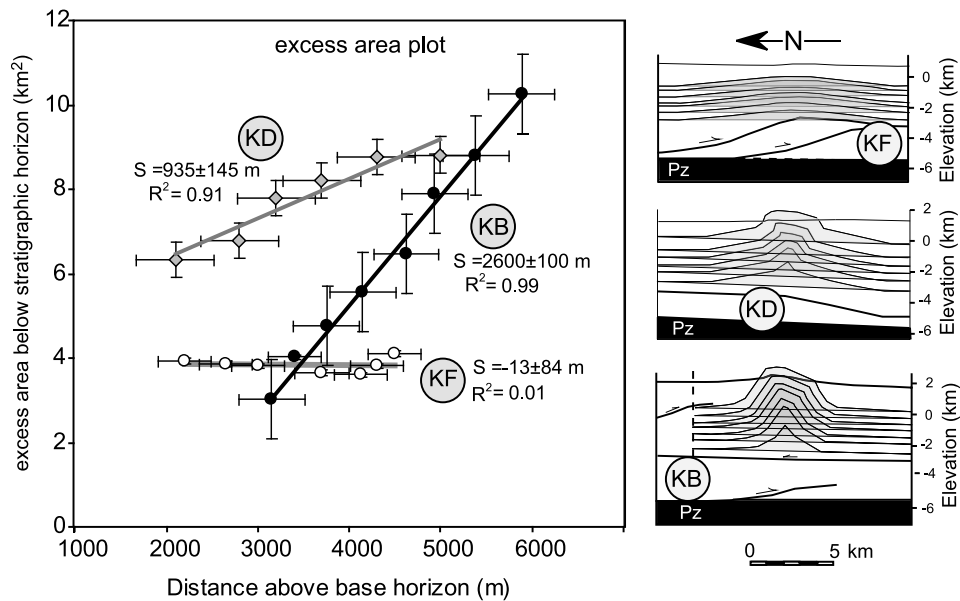


Figure 9. Graph of “excess area” beneath mapped horizons for cross sections KF, KD, and KB and the distance above the interpreted basal detachment. Only stratigraphic levels above the uppermost interpreted detachment horizon were used in the analysis, and the data were plotted based on their height above the lowest interpreted detachment horizon. Errors for the data points are assigned following the methodology of *Gonzalez-Mieres and Suppe [2006]*. The slope of the line formed by the data from any one fold indicates the total shortening across the fold [*Epard and Groshong, 1993*]. Horizons used for the shortening calculation are indicated on their respective cross sections.

these folds. We assume that any pure shear below these depths matches the shortening within the upper competent layers, but all estimates are likely minima due to undetermined shortening accommodated via horizontal compaction of sediments [Gonzalez-Mieres and Suppe, 2006]. Our excess area plots, however, cannot be used to constrain the depth to the detachment because material is likely added into the core of the anticline due to evaporitic flow and faulting within the detachment horizons.

[35] For the Kashi fold, undeformed strata from both sides of the fold are parallel to the underlying detachment level and match regional stratigraphic gradients of 1° – 3° , similar to active fan surfaces. We calculated the excess area from at least seven stratigraphic horizons from Kashi West (KB), the water gap (KD), and the eastern topographic tip (KF), respectively (Figure 9). Least squares regressions through data points from an individual fold indicate shortening of 2600 ± 100 m, 935 ± 145 m, and -13 ± 87 m for KB, KD, and KF, respectively (Figure 9 and Table 2). The r^2 values of 0.91 for the water gap and 0.99 for Kashi West indicate a good linear fit to the data, supporting concentric folding in the upper levels. In contrast, at the eastern topographic tip (KF) the r^2 value of 0.004 is extremely low, because the shortening magnitude is too small to measure confidently. Line length estimates for the eastern tip range between 46 and 64 m with a mean of 54 ± 5.5 m. This shortening estimate of ~ 50 m is consistent within error of our excess area determination (Figure 9) and also with measured shortening of 0.2–0.7 km measured at ~ 10 km west of KF by Scharer *et al.* [2004] (section G-G', see Figure 3g for location).

5.2. Growth and Propagation of the Kashi Anticline

[36] The Kashi anticline exhibits a strong longitudinal asymmetry. Although the fold is doubly plunging, its lateral propagation appears to have been asymmetric with more rapid eastward than westward propagation. For the purposes of clarity, we will discuss changes along the fold in terms of kilometers from the western topographic end of the fold (Figure 10). Instead of lying halfway along the fold, the structural crest is located between 5 and 15 km from the western tip based on our cross sections, surface mapping data from Kang *et al.* (unpublished manuscript, 1978), and the longitudinal profile of the fold (Figures 3, 10b, and 10c). Furthermore, the western geomorphic termination of the fold is a blunt, steeply plunging ($\sim 7^{\circ}$), broad fold nose (Figure 10), whereas the eastern termination is an elongate, gently plunging arc whose axis dips at 1.8° across the last 7 km of the topographically expressed fold nose (Figure 10c).

[37] We can estimate the position of the modern eastern structural tip with three approaches: shortening gradients, structural plunge, and seismic data. First, we estimate the position of the tip based on the gradient of shortening along the fold. Our three cross sections (Figures 3 and 11a) define a decrease in shortening gradient toward the eastern tip. Although some of this change could be due to errors in our shortening estimates, we prefer to accept the calculated change in shortening and infer that shortening should decrease to zero at a point east of the eastern tip that can be quantified from the shortening gradient. Linear regression through the data points yields an average shortening gradient of ~ 57 m/km ($r^2 = 0.94$). Linear fits between

adjacent cross sections produce a shortening gradient between Kashi West (KB, 16 km) and the water gap (KD, 36 km) of ~ 83 m/km, and between the water gap and the eastern tip (KF, 60 km) of ~ 37 m/km (Figure 11a). Because shortening toward the east appears to decrease nonlinearly, we use a logarithmic regression through these three points that provides a good fit to the data and yields maximum and minimum shortening gradients between 117 and 33 m/km with an r^2 of 0.99 (Figure 11a). The gradient at the eastern topographic tip thus ranges between 57 and 33 m/km. We, therefore, estimate that shortening decreases from 54 m at the section KF (eastern tip at 60 km) to 0 between 61 and 62 km. Second, we utilize the uplifted and folded topographic tip of the fold to define its axial plunge where the resistant Xiyu conglomerate is preserved across the fold's nose. The resistant layer can be projected east into the subsurface on seismic line TA9410 (Figure 11c) and is observed leveling out to horizontal at $\sim 350 \pm 100$ m depth (0.85 ± 0.1 km elevation above sea level, Figure 11b). We, therefore, project the east plunging beds to the level where they are interpreted to flatten out, thereby predicting the current location of the fold nose. This projection, incorporating a range of plunges between 1.6° and 2.0° for the fold nose, predicts the tip of the fold lies between 65 and 83 km. Third, the longitudinal seismic line TA9410 parallels the fold's northern flank (Figures 3g and 11c), clearly shows a flattening of dips (growth strata) between 75 and 82 km, and likely corresponds to the nose of the Kashi anticline. In addition, seismic line TA9403 (Figures 4c and 4d) ~ 22 km farther east of the KF (eastern topographic nose) shows gently north dipping beds where the north flank of the extended Kashi anticline would be present. These gently dipping beds dip $< 3^{\circ}$ and may be depositional, not structural, in origin. The dips to the north, however, are anomalous in this part of the basin where the depositional gradient is 1° – 3° to the south. Given their coincident location along strike of the north flank of the Kashi fold, we interpret these beds to be structurally controlled and to represent the incipient fold's buried northern flank at 81 km (Figure 11c). Taken together, these three estimates and the north dipping beds from TA9403 indicate the total length of the fold is between 62 and 82 (72 ± 10) km, of which only the westernmost 60 km is emergent. Even though the overall topographic gradient in this part of the foreland slopes to the southeast (Figures 1 and 12), modern drainage patterns diverge along the projected, but buried, crest of the fold and suggest that gentle folding of the modern surface is influencing river gradients. These rivers converge just east of where we project the tip of the fold (Figure 12).

[38] Using the age of growth strata, we can estimate the lateral propagation rate of the fold toward the east. If we assume that fold growth initiated at $1.4_{-0.2}^{+0.17}$ Ma at Kashi West (KB, 16 km) and propagated east to its termination at 72 ± 10 km, then the average eastward propagation rate would be 40 ± 7 km/Myr, similar to estimated lateral propagation rate of 50 km/Myr for the Atushi-Talange anticline [Scharer *et al.*, 2004]. For the Kashi fold, this average rate can be subdivided, because when the structural cross sections are considered in the context of the age constraints, the growth of the anticline as a topographic feature is neither spatially nor temporally uniform. Instead, we propose a three-phase growth model whereby the

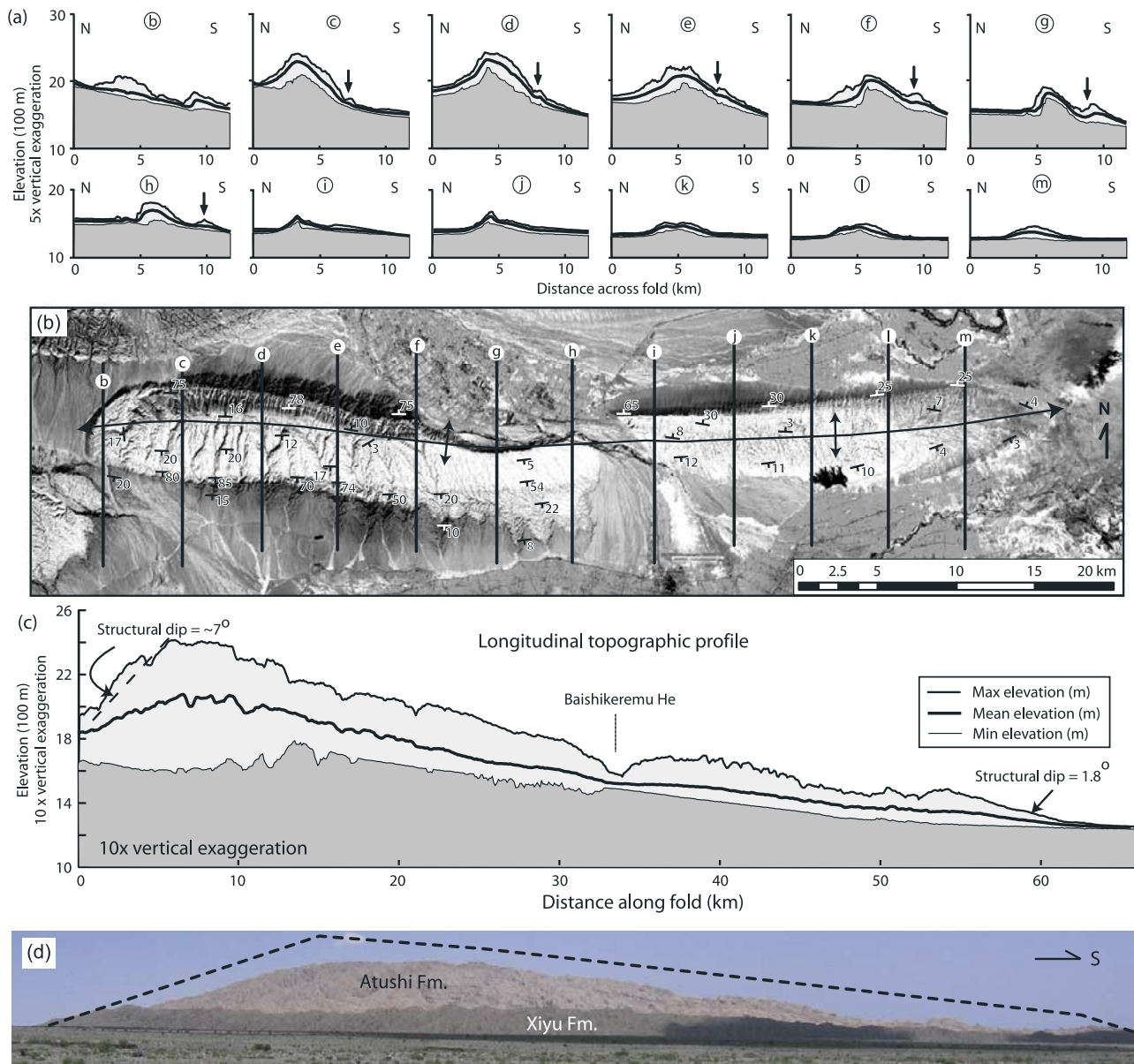


Figure 10. Topographic analysis based on 90-m SRTM data of the Kashi fold. (a) Cross section profiles based on 5-km-wide swaths (2.5 km to either side of the cross section lines). Darker gray shaded areas are below the minimum elevation value within each swath; the light gray shaded area represents the maximum topographic relief of the fold at each section. Thick black lines show the average elevation. Arrows mark the location of conglomeratic beds, which typically define the local maximum topography on the fold’s flanks. Note that the stratigraphic level of the contact between the Xiyu conglomerate and Atushi Formation is higher along strike and relatively younger eastward on the south limb from cross section profiles c to h. (b) Landsat 7 image of the Kashi fold with center of each 5-km-wide swath (cross section) location indicated. Representative flank dips from our surface mapping and Kang et al. (unpublished manuscript, 1978) are shown along fold strike. (c) Longitudinal profile of a swath 12 km wide along the crest of the Kashi fold, with a gentle taper pointing eastward in the direction of fold propagation. Dip (structural plunge) of the pregrowth strata at each end of the fold is shown. (d) Photograph of west nose of the Kashi anticline showing north vergence of the fold. View is to the east. The darker gray rim around the anticline is the conglomeratic and fairly resistant Xiyu Formation. The Atushi Formation (light color) exposed by the anticline is easily eroded by ephemeral streams.

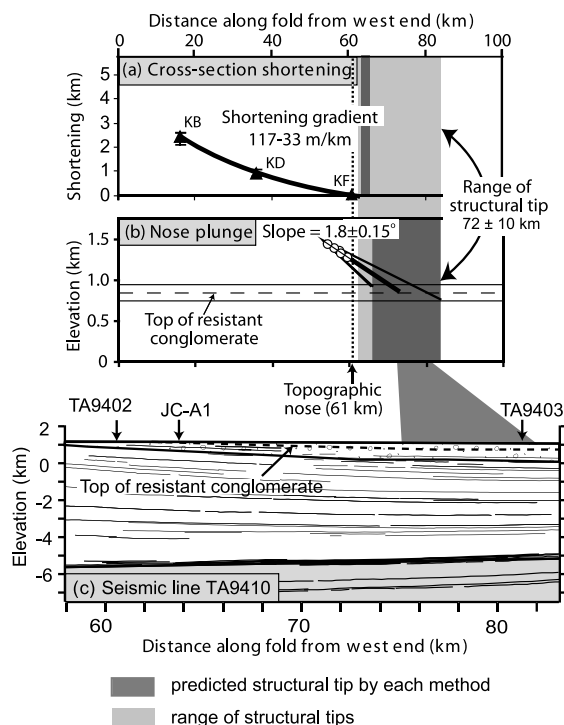


Figure 11. Methods for projecting the eastern tip of the Kashi fold. (a) Extrapolation of shortening gradient to 0. Best fit curve through points is a logarithmic regression and predicts 62 km for the total length of the Kashi fold. (b) Topographic plunge of the Kashi fold nose (from Figure 14) where uneroded, resistant conglomerate strata are extrapolated to an elevation of 0.85 ± 0.1 km (dashed horizontal line): The depth these strata become horizontal in seismic line TA9410. Dotted lines are the standard error of the regression through the digital elevation model data and constrain the possible range of dips for the fold nose. The intersection between the plunging nose and 0.85 ± 0.1 km indicates the fold nose should occur between 64 and 82 km. Open circles locate topographic cross sections v, w, x, y, and z (see location on Figure 14d). (c) Line drawing interpretation of longitudinal seismic line TA9410 (see Figure 3g for location). The line drawing clearly shows a flattening of dips between 75 and 82 km from the west, consistent with our interpreted fold nose at $\sim 72 \pm 10$ km from the west end of the Kashi Anticline. Dashed reflector is the top of the resistant conglomerate that flattens at a depth of ~ 350 m below the ground surface. Note that the scale indicating distance from west is different for Figure 11c than Figures 11a and 11b.

western end of the Kashi fold grew symmetrically from approximately 1.4 to 1.1 Ma, the fold rapidly lengthened eastward between 1.1 and 0.8 Ma, and then tip propagation slowed to the present. Whereas the reason for the asymmetric and uneven fold propagation is unknown, we speculate that propagation of the western tip was inhibited by the presence of the Mingyaole anticline [Scharer *et al.*, 2004]. Interference between propagating faults has been shown both to reduce tip propagation and to augment the axial plunge of the fold tip via continuing slip accumulation, thereby creating an asymmetric fold geometry like that of

the Kashi anticline [Cowie *et al.*, 2000; Gupta and Scholz, 1998].

[39] The difference in the magnetostratigraphic ages (Figure 5) between the growth strata at Kashi West (KB at 16 km, $1.4^{+0.17}_{-0.2}$ Ma) and those at Kashi Town (KC at 29 km, 1.07 ± 0.03 Ma) sections define an average propagation rate of $\sim 39^{+91}_{-15}$ km/Myr between them, based on their horizontal separation (13 km, Figure 13). The large uncertainty on the rate is due to the small spatial and temporal separation of the dated sections and the relatively large age uncertainties that results from inexact correlation of the Kashi West magnetostratigraphy and the unknown temporal position of any strata within a given magnetozone. By combining the well-constrained growth strata (1.07 ± 0.03 Ma) at km 29 (KC) with the 0.8 ± 0.3 Ma age at the eastern topographic end of the fold (60 km at KF), we can define a second interval of lateral fold propagation rate at 115^{+402}_{-63} km/Myr eastward between Kashi Town (KC) and the eastern tip (Figure 13). Because the maximum age at the eastern emergent tip overlaps the minimum age at KD (Kashi Town) section, this calculated propagation rate also has large uncertainties. Since $\sim 0.8 \pm 0.3$ Ma, the fold has propagated <22 km east to its eastern tip at a rate of 15^{+29}_{-13} km/Myr (Figure 13). Whereas a steady propagation rate of 70–120 km/Myr is possible (given the age uncertainties) from the initiation of fold growth until ~ 0.8 Ma, the data favor two stages: slower propagation until ~ 1.1 Ma and then considerably faster until 0.8 Ma. Since ~ 0.8 Ma, the rate of tip propagation has greatly slowed.

[40] At km 16, where we have independent magnetostratigraphic age control on the growth strata at cross section KB (Kashi West) and can calculate the structural relief above the detachment level (Figure 9), the average rate of vertical fold growth is $1.8^{+0.4}_{-0.3}$ km/Myr (Table 2). If we interpolate the age of initial fold growth for any location along the fold from the Kashi West section to its eastern tip, we can estimate rates of differential rock uplift and horizontal shortening for cross sections at the water gap (KD; 36 km) and the emergent eastern tip (KF; 60 km) (Figure 13). These calculations define an average vertical uplift rate of $1.9^{+0.5}_{-0.3}$ km/Myr since $1.0^{+0.08}_{-0.1}$ Ma at KD and of $0.6^{+0.6}_{-0.3}$ km/Myr since 0.8 ± 0.3 Ma at KF (Table 2). These differences along the fold indicate that the rate of vertical growth decreases eastward. Similarly, the average shortening rate of $1.7^{+0.5}_{-0.4}$ km/Myr at the Kashi West section (KB; 16 km) is greater than the rates of $0.95^{+0.3}_{-0.2}$ km/Myr and $0.06^{+0.06}_{-0.03}$ km/Myr for the water gap (KD; 36 km) and eastern tip (KF; 60 km), respectively (Table 2). This along-strike reduction in shortening rate is not unexpected: A similar trend is observed in the Atushi-Talange anticline to the north [Scharer *et al.*, 2004], and such change can produce the longitudinal displacement gradients that are characteristic of both normal and thrust faults [Davis *et al.*, 2005; Dawers and Anders, 1995]. Although the shortening rate decreases to the east, however, the ratio of the rate of rock uplift to both the shortening rate and the total shortening increases about tenfold toward the eastern tip, reinforcing observations elsewhere that the most rapid changes in structural relief occur in the incipient stages of folding when limb rotation is the dominant growth mechanism [Hardy and Finch, 2005; Hardy and Poblet, 1994; Poblet and McClay, 1996; Rockwell *et al.*, 1988].

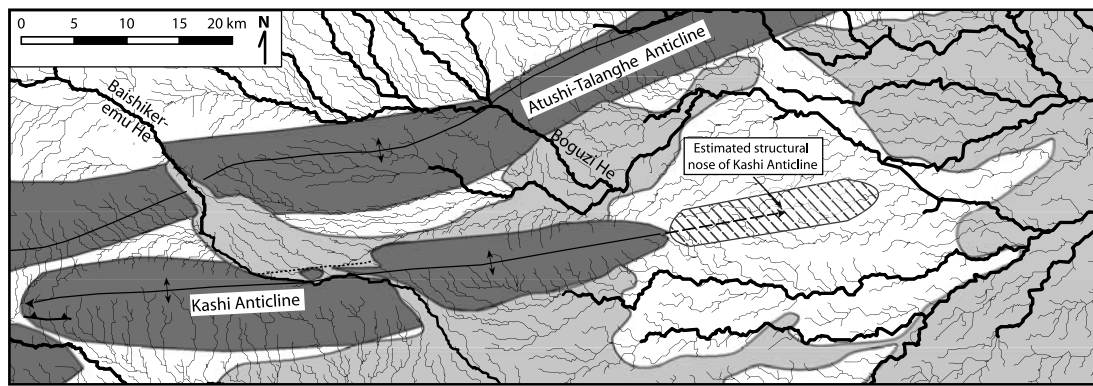


Figure 12. Drainage patterns of the Kashi area and the projected axis and tip position of the buried Kashi fold. Thick black lines represent drainages greater than 50 km². Thin black lines represent drainages with >1 km² and <50 km². Exhumed Plio-Pleistocene strata (dark gray shading) form the core of the topographically expressed Kashi and Atushi-Talanghe anticlines. Dashed region represents possible location of structural nose. Quaternary fluvial deposits are distinguished between active (light gray) and largely inactive (white).

[41] For the Kashi fold, the ratio of the maximum reconstructed shortening to fold length is $\sim 3 \times 10^{-2}$: a displacement-length ratio that is typical of thrust faults [Elliott, 1976; Scholz, 2002]. The rate changes along the Kashi fold, however, do not produce the semielliptical or bell-shaped displacement gradients suggested to typify many faults and fault zones [Cartwright *et al.*, 1996; Dawers and Anders, 1995]. Instead, both the total shortening and the shortening rates suggest higher initial rates of shortening toward the structural apex of the fold (km 5–15) leading to significant accumulation of displacement to the west of the water gap (KD; 36 km) prior to an interval of lateral propagation extending past the emergent fold tip (KF; 60 km) and accompanied by slower rates of shortening (Figure 13). A three-phase model for growth of the Kashi anticline is also supported by the reconstructed fold shape based on interpolation between the structure sections (Figure 3): The western half of the emergent fold suggests significantly greater shortening than does the eastern half.

[42] The causes of the acceleration in the eastward fold propagation rate after ~ 1.1 Ma or of the abrupt decrease in rate after ~ 0.8 Ma are unknown. We speculate that the acceleration occurred when the detachment exploited a particularly weak, evaporate-dominated horizon and that once the detachment reached the stratigraphic termination of this weak layer, the rate abruptly decreased.

5.3. Tectonic Geomorphology and Drainage Patterns

[43] The present morphology of the fold is controlled by three interacting elements: the amount of shortening, the rates of structural uplift minus the basin sedimentation, and the erodability of the bedrock. Higher topography and greater relief are associated with (1) zones of greater total shortening, (2) more rapid and sustained uplift relative to the basin sedimentation, and (3) rocks that resist erosion. On the basis of analysis of a 90-m digital elevation map (DEM), the along-strike fold morphology reflects its temporal evolution (Figure 10). The western half of the fold, where total shortening and average shortening rates are highest, has a more prominent topographic expression,

attaining a height some 900 m above the adjacent plain. In contrast, many of the cross sections in the eastern half of the fold show <200 m of topographic relief. The fold has a roughly constant width along strike, indicating that much of the shortening on the west half was accommodated by developing structural relief. The highly asymmetric nature of the fold along strike is revealed by the blunt western and gently tapered eastern topographic tips (Figure 13) and by the topographic culmination in the westernmost sector of the fold (Figure 10c). Our inference of three-stage fold growth is reinforced by the trends of both the mean and maximum topography. The topographic gradient descends eastward more steeply across the western half of the emergent fold before flattening dramatically across the eastern half. Maximum, minimum and mean surface elevation profiles show a subtle decrease in slope between 25 and 30 km (Figure 13b). These decreases occur where we interpret an eastward change toward more rapid lateral propagation and slower differential rock uplift.

[44] Of the two lithostratigraphic units that are exposed on the fold flanks, the Xiyu conglomerate is considerably more resistant to erosion than are the Atushi sandstones and siltstones. This contrast exerts a fundamental control on the mesoscale topography of the Kashi fold. At the eastern nose of the anticline, the influence of rock strength on erosion is most clearly evident. As the conglomerate-covered nose of the fold emerges above the depositional plain, only very minor dissection occurs, such that topographic cross sections across the fold reveal its pristine structural shape (Figure 14). Not until ~ 200 m of topographic relief is attained are slopes sufficiently steep and long to permit dissection and erosional removal of the conglomerate. Once the carapace of conglomerate is breached, erosion accelerates and attacks the weak rocks in the core of the fold. This change is clearest in the longitudinal topographic section where the highest part of the pristine nose corresponds with the edge of preserved conglomerate (Figure 14). Along the remainder of the fold, conglomeratic strata form resistant ridges of locally higher topography encircling the fold,

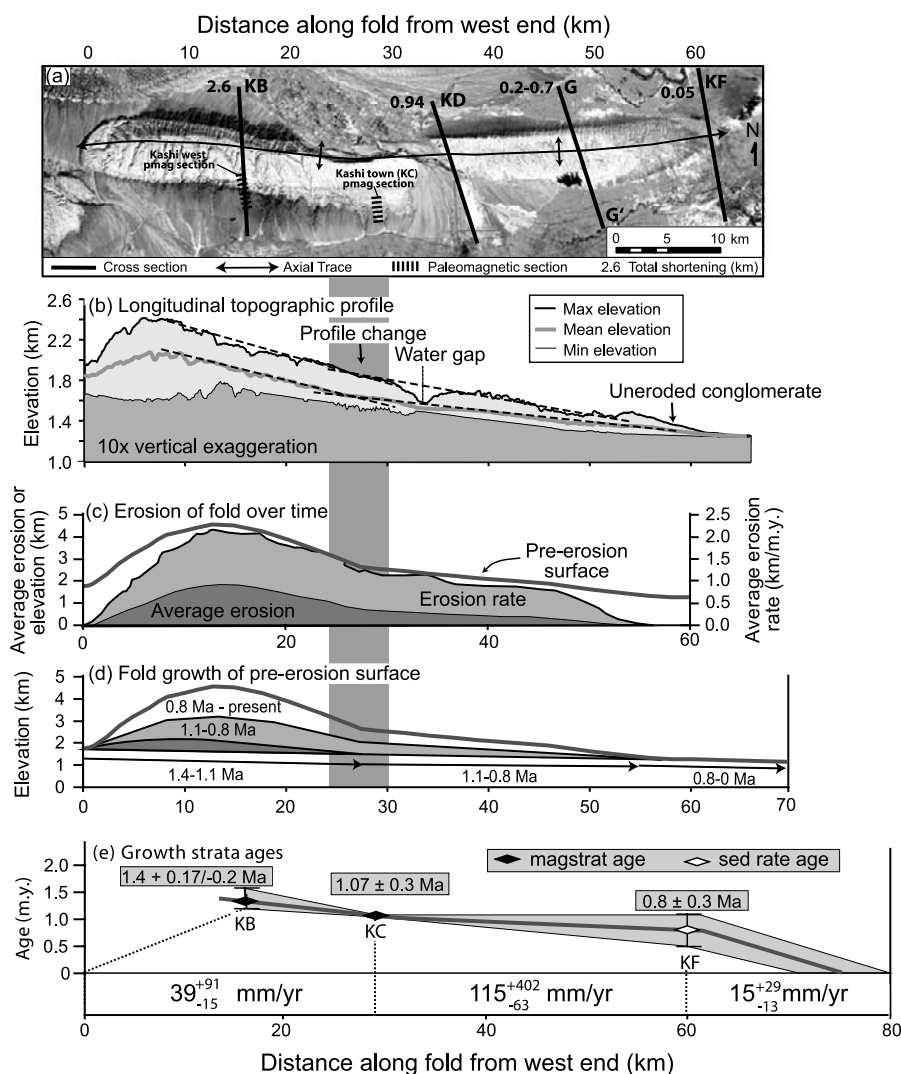


Figure 13. Indicators for the evolution of Kashi fold growth. (a) Landsat image of the Kashi fold showing cross section locations and increased dissection of the fold surface between 0 and 20 km. Cross section G-G' is from Scharer *et al.* [2004]. (b) Maximum, minimum, and mean surface elevation profiles showing divergence toward the west. (c) Estimates of erosion, erosion rate, and preerosion elevation for the length of the Kashi anticline. A preerosion surface was created based on dip data along the fold and on the highest (youngest) pregrowth strata in each of the three structure sections in Figure 3. This profile exhibits a noticeable change at 20–25 km. The present-day topography was subtracted from this preerosion surface to define the total erosion for each 90-m pixel in the digital elevation model. (d) Reconstruction of three-stage growth of the fold in the absence of erosion. (e) Lateral propagation rate calculations (based on dated growth strata, Figure 5) yielding an estimate of $\sim 39_{-15}^{+91}$ km/Myr between Kashi West (KB, 16 km) and Kashi Town (KC, 29 km) and 115_{-63}^{+402} km/Myr between Kashi Town and the eastern tip (KF, 60 km). Lateral propagation rates would drop to 15 ± 12.5 mm/yr for the fold to propagate to 72 ± 10 km for the last 0.8 Myr. Growth strata ages are based on magnetostratigraphy from Kashi West (KB) and Kashi Town (KC) and on extrapolated deposition rates of 550–840 m/Myr for the eastern tip (KF).

except where eroded adjacent to the major water gap (see Figure 10 for examples).

[45] Although it is impossible to pinpoint when the Baishikeremu He became trapped in its current water gap (Figures 1 and 12), its prominent eastward deflection along the northern flank of the fold and its position at the transition from steeper to gentler topographic gradients suggests it was trapped when the phase of rapid lateral

lengthening of the fold began. Upstream of the water gap, the Baishikeremu He impinges on the north limb of the fold and has beveled laterally into it. Such erosion tends to remove the outer, Xiyu conglomeratic strata of the fold. Given that the Xiyu rocks are most resistant to erosion, the river may be able to sustain its course more readily through a water gap across the growing fold once the resistant marginal rocks are removed. The eastward deflection of

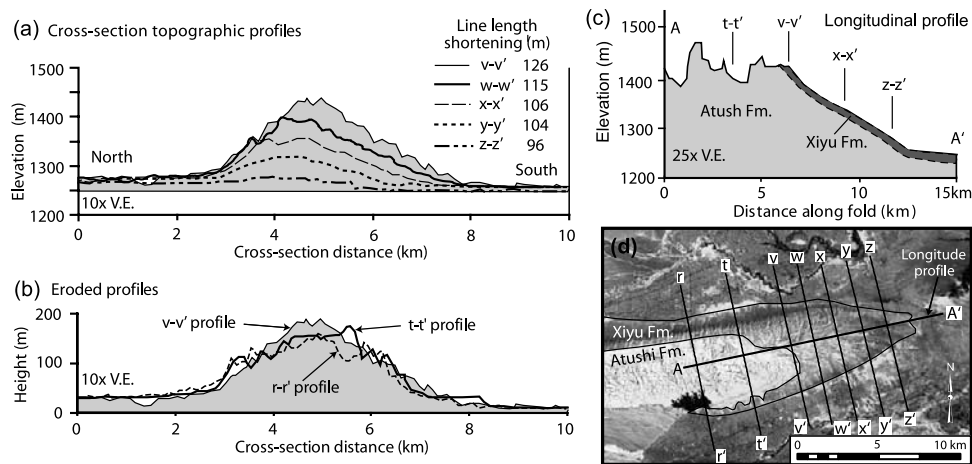


Figure 14. Topographic profiles from the eastern nose of the Kashi fold. (a) Cross section topographic profiles spaced at 1.5 km distance along the uneroded nose of the Kashi anticline. These clearly depict the increasing amplitude and shortening westward and north vergence of the pristine fold. (b) Cross section profiles $r-r'$, $v-v'$, and $t-t'$ showing the uneroded and eroded section of the Kashi fold. Note the lowering of the fold crest by erosion. In the absence of erosion, profiles $r-r'$ and $t-t'$ would be expected to be ~ 80 m and ~ 160 m higher than profile $v-v'$. (c) Longitudinal profile of the eastern Kashi anticline nose showing selected topographic profile locations. The resistant Xiyu conglomerate is shown schematically in relation to the Atushi Formation. (d) Landsat image of the eastern Kashi anticline nose, showing all topographic profile locations.

the Baishikeremu He along the north limb of the fold suggests that an eastward topographic gradient existed to deflect the stream before it could breach the Xiyu carapace [e.g., Jackson *et al.*, 1996].

[46] In order to examine along-strike changes in erosion, we reconstructed the three-dimensional structural surface representing the shape of the pre-growth strata in the absence of erosion. The mean erosion across the fold at any point along its length ranges from nearly 2 km at the western structural culmination, to <700 m across the eastern half of the topographically expressed fold, and finally to near 0 where the conglomerate is preserved across the fold's nose (Figure 13). The asymmetry of both the pre-erosion surface and the mean erosion is interpreted to support the three-step fold growth model. Along-strike ages are estimated using the defined lateral propagation rate of 39 km/Myr from 0 to 29 km, 115 km/Myr from 29 to 60 km, and 15 km/Myr to the fold tip at $\sim 72 \pm 10$ km.

[47] Folding is interpreted to have begun at 0.8 Ma near the presently emergent fold tip. Since then, the Kashi anticline's eastern (buried) tip propagated as much as ~ 22 km and grew vertically, but not at a rate exceeding the rate of deposition. Only after shortening of ~ 50 m and development of ~ 500 m of structural relief does the fold begin to achieve a topographic expression. Topographic profiles across the emergent tip (Figure 14) reveal the north vergence of the incipient fold as shown by the elongate southern limb and steeper northern limb. As noted above, little erosional modification of the fold shape occurs until ~ 200 m of topographic relief is attained. Once erosion breached the Xiyu conglomerate, erosion rates rapidly accelerated across a distance of ~ 10 km (from approximately km 58 to 48, Figure 13c).

[48] Compared to the western half of the emergent fold, erosion rates are steadier in the eastern half. The divergence of the mean and maximum topography in this part of the fold, however, indicates that total erosion increases westward (Figure 13). The spatially uniform difference between the mean and minimum elevation suggests the fold has approached a topographic steady state in the east, such that erosion balances rock uplift and topography shows little sensitivity to the total amount of erosion or the erosion rate in this sector. In the western half of the fold, total rock uplift, average erosion, and erosion rates all accelerate (Figure 13) in concert with the increased magnitude of reconstructed shortening in the same region (Figure 3). Not unexpectedly, the highest erosion rate (~ 2.4 km/Myr) is associated with the greatest total erosion, just near the structural culmination. In general, about 75% of the rock that is raised above local base level is subsequently removed by erosion. Despite this intense erosion, the morphology of the fold broadly mimics spatial variations in the magnitude of structural shortening and differential rock uplift (Figures 10a and 10c).

[49] Evidence for the eastward propagation, northward vergence, and a buried fold tip to the east of the emergent fold is apparent in drainage patterns (Figure 12). The channels along the southern limb of the fold are commonly deflected toward the east within the folded domain, especially in the eastern half of the fold. Such a deflection is consistent with channels initially responding to slopes imposed by the topographic emergence of the fold tip and then being incised as stable channels that trend a bit obliquely to the present dip of the fold limb [Jackson *et al.*, 1996]. The north-south drainage divide is consistently displaced toward the north as would be expected for an actively growing, north vergent fold with an elongate,

gently dipping southern limb. Finally, rivers diverge along the eastward, buried projection of the fold tip. Despite the subtle topographic expression of the buried fold, river channels are oriented obliquely away from the fold axis and rarely cross it. After crossing the Atushi-Talanghe anticline, the Boguzi He channel abruptly deflects back toward the northeast: a deflection that we also interpret as a response to the growth of the buried Kashi fold.

6. Constraints on the Growth Mechanism and Kinematic History

[50] Our stratigraphic observations indicate the presence of moderately thick gypsiferous layers at several levels within the Tertiary strata, which provide likely horizons for detachment. The previously reviewed structural data reveal both forelimb and back limb rotation [Scharer *et al.*, 2006], a box-like fold geometry for some cross sections, and no significant surface faulting. The seismic sections depict several key attributes of the structural style. First, the dip of the basement strata is low, but varies by a few degrees either to the north or south. Second, low-angle detachments appear to occur both at the base of and within the Tertiary strata at depths ranging from 4 to 7 km. Third, both north and south vergent thrusts and some incipient duplexes disrupt the lower 3 km of Tertiary strata. Fourth, the style of broad folding in the upper 4 km is only weakly coupled to the style in the underlying rocks. Thickness changes in some beds above the low-angle faults suggest flow within the core of the folds. Fifth, limb rotations in the folds that are manifested at the surface appear unrelated to specific faults in the subsurface. Sixth, strong along-strike variations in limb dip ($<9^\circ$ to $>65^\circ$, see Figure 10b) suggest that southern limb steepens during folding.

[51] Southern limb rotation and the decoupling of the folding geometry from the underlying faults are inconsistent with the common predictions of fault propagation or fault bend folding [Suppe, 1983; Suppe and Medwedeff, 1990]. However, limb rotation can occur due to (1) changes in bed thickness during fault propagation folding, (2) layer-parallel shear during fold amplification [Mittra, 1990], (3) material friction and dilation during trishear folding [Cardozo *et al.*, 2003], or (4) translation over a curved fault [Suppe *et al.*, 1997]. Overall, however, the sum of the seismic, stratigraphic, and structural observations support the interpretation of the Kashi fold as an asymmetric detachment fold.

[52] Along the Kashi anticline, the cross sections have a similar shape comprising a tightly folded core developed over shallowly dipping outer flanks, except at its east tip (Figure 3). In general, total shortening reduces to the east along the strike of the fold (Figure 3). Both seismic surveys and topography indicate that fold width remains fairly constant along strike but that fold heights and limb dips correlate with increased shortening [Scharer *et al.*, 2004; Kang *et al.*, unpublished manuscript, 1978]. Cross sections with greater total shortening exhibit longer steeply dipping kink bands and greater fold amplitudes. Growth strata on the outer edges of the fold are fanning: a geometry consistent with limb rotation [Poblet *et al.*, 1997] or curved hinge zone migration [Suppe *et al.*, 1997]. All these indicate that both limb lengthening and limb rotation play a role in fold growth: processes similar to what is observed in Hardy and

Finch's [2005] and Mitra's [2003] detachment models. Similarity of the fold forms along strike suggests that the general shape of the fold is developed early and is subsequently amplified throughout the history of the fold, but not in a purely self-similar style. Continued shortening is accommodated, in part, by increasing in the length of the steeply dipping kink bands and by episodically shifting the limited activity hinges outward with time. This interpretation is supported by the increase in fold amplitude with continued shortening and by the geometries of folded terraces that remain undeformed as they cross formerly active hinges [Scharer *et al.*, 2006]. Planar, rotated terraces indicate more recent folding is accommodated by block rotation of the limbs. The width of the folds are maintained by translation of pregrowth bedding across the outermost hinges and up into the shallowly dipping flanks, which also preserves growth strata on the outer flanks of the fold [Scharer *et al.*, 2006].

[53] Our structural reconstructions indicate that the rate of shortening on the Kashi anticline slowed as the fold tip propagated eastward during the past 1 Myr. This slowing may result from interplay with the Atushi-Talanghe fold that lies 10–20 km north of the Kashi anticline. Magnetostratigraphically dated growth strata from the Atushi-Talanghe fold [Chen *et al.*, 2002] indicate it also began to grow by 1.2 Ma in its eastern half, north of the present eastern topographic tip of the Kashi fold. Subsequently, the Atushi-Talanghe fold propagated another 30 km to the east. Although no direct temporal control exists for the more westerly part of the Atushi-Talanghe fold, a balanced section through its thick, near-vertical limbs [Scharer *et al.*, 2004] suggests two attributes. First, the steep limbs may have inhibited additional shortening. "Locking up" of the Atushi-Talanghe fold may have prompted the initiation of fold growth in the Kashi anticline directly to its south. Second, more shortening occurred in the western Atushi-Talanghe fold than farther east along it. The progressive structural tightening of the eastern Atushi-Talanghe fold over the subsequent million years may have accommodated more of the regional contraction and, in turn, retarded the magnitude of shortening in the Kashi anticline lying south of the eastern propagating Atushi-Talanghe fold. Additional time control and balanced sections are needed to assess details of the rate of shortening along the Atushi-Talanghe fold and its interactions with the Kashi fold.

7. Conclusion

[54] Growing anticlines are a common structural manifestation of the migration of deformation into a foreland basin. Despite their ubiquitous presence, few studies have sufficient temporal control on a single fold to delineate rates of structural and topographic growth or to elaborate the relationships between amplifying topography and erosion. Here, we have used two new, along-strike magnetostratigraphic sections and seismic data to place time constraints on the Quaternary structural and geomorphic evolution of the Kashi fold in the foothills of the southwestern Tian Shan. This magnetostratigraphy allows us to define the age of growth strata for three locations along the fold that delineate both the onset of deformation at each section and rate of propagation of the fold between them. Fold

growth initiated at ~ 1.4 Ma. Calculations of the amount of shortening and differential rock uplift define an asymmetric growth history with two characteristics. First, growth of the adjacent Mingyaole anticline to the west inhibited the westward propagation of the fold tip, such that the tip stabilized and the fold nose simply accumulated slip. Second, displacement accumulated more rapidly in the early stages of fold growth (from approximately 1.4 to 1.1 Ma) only in the western half of the fold. After the first 0.3 Myr when the folding propagated eastward at ~ 39 km/Myr, the fold rapidly lengthened and grew to its present eastern topographic tip between 1.1 and 0.8 Ma. Since 0.8 Ma, the fold has slowly propagated < 22 km farther east to its current structural tip. The fold thus appears to have grown in three stages with less shortening and propagation during the latter half of its growth.

[55] The structure of the Kashi anticline and the geometry of its growth strata result from deformation of a faulted detachment fold that formed within the thick Neogene deposits of the foreland. Numerous dip panels separated by abrupt kink bands define the overall fold shape. Drainage divides and stream patterns reflect both the asymmetry of the fold and its lateral propagation over the past million years. The eastern nose of the Kashi anticline has no topographic expression: Differential uplift rate of its buried nose has been insufficient to outpace the rate of sediment accumulation across the fold's flanks.

[56] The topography of the emergent fold is a function of two key controls. First, the large-scale topographic relief reflects the total shortening at any point along the fold. Second, the duration of exposure and the relative resistance to erosion of folded and differentially uplifted rocks determine smaller-scale topographic characteristics. Xiyu conglomerate forms a carapace enveloping the newly emergent fold nose. No significant erosion of the nose occurs until ~ 200 m of topographic relief develops. With continued fold growth, the conglomerate is stripped and weaker Atushi Formation sandstone and siltstone is removed from the core of the fold, leaving conglomeratic flatirons and ribs defining the rim of the fold. Although the amount of erosion varies by $> 700\%$ from east to west along the eastern half of the fold, the average erosion rate varies by $< 50\%$ and the mean topographic relief remains uniform. Hence, once the resistant conglomerates are breached, the fold erodes about as rapidly as rocks are raised above the local base level, such that approximate steady state topography is achieved. If the western half of the emergent Kashi fold were also in steady state, it would imply that the early gradients in differential shortening and crestal uplift were sustained throughout fold growth, such that more rapid rates of erosion correspond with zones of higher relief and more rapid rock uplift. Inferences of higher differential uplift rates in the western part of the Kashi fold are supported by deformed terraces that dip toward the propagating eastern nose [Scharer et al., 2006].

[57] Combinations of high-resolution chronologies, structural mapping and section reconstruction, and analysis of digital topography permit the structural and geomorphic evolution of a fold to be placed in a reliable temporal framework. With such time control, it becomes possible to examine rates of lateral and vertical propagation, to quantify

erosion rates, and define the time and magnitude of deformation required to overcome some geomorphic thresholds.

[58] **Acknowledgments.** This research was supported by National Science Foundation of China grants 40672109 and 40372081 and by the Continental Dynamics and Tectonics program of the US NSF (EAR 961476, 0230403). J. Chen thanks DAAD for a scholarship of support of his visit to GFZ paleomagnetic laboratory. J. Chen is especially grateful to J. L. Kirschvink at Caltech and N. R. Nowaczyk at GFZ for the use of the paleomagnetic laboratory and to N. R. Nowaczyk, J. L. Kirschvink, and B. Kopp for help with paleomagnetic techniques and interpretation. We greatly appreciate Sun Dongjiang, Feng Wenquan, and Patricia Ruano for their dedicated assistance in the field. We made extensive use of software provided by Craig Jones and N. R. Nowaczyk, for the analysis and presentation of paleomagnetic data. Critical and thorough reviews of the manuscript by J.-P. Avouac and two anonymous reviewers significantly improved the current version.

References

- Abbott, L. D., E. A. Silver, R. S. Anderson, R. Smith, J. C. Ingle, S. A. King, D. Haig, E. Small, J. Galewsky, and W. Sliter (1997), Measurement of tectonic surface uplift rate in a young collisional mountain belt, *Nature*, *385*, 501–507.
- Abdrakhmatov, K. E., R. Weldon, S. Thompson, D. Burbank, C. Rubin, M. Miller, and P. Molnar (2001), Origin, direction, and rate of modern compression in the central Tien Shan, Kyrgyzstan, *Geol. Geofiz.*, *42*, 1585–1609.
- Abdrakhmatov, K. Y., et al. (1996), Relatively recent construction of the Tien Shan inferred from GPS measurements of present-day crustal deformation rates, *Nature*, *384*, 450–453.
- Allen, M. B., S. J. Vincent, and P. J. Wheeler (1999), Late Cenozoic tectonics of the Kepingtage thrust zone: Interactions of the Tien Shan and Tarim Basin, northwest China, *Tectonics*, *18*, 639–654.
- Armstrong, F. C., and S. S. Oriol (1965), Tectonic development of Idaho-Wyoming thrust belt, *AAPG Bull.*, *49*, 1847–1866.
- Avouac, J.-P., P. Tapponnier, M. Bai, H. You, and G. Wang (1993), Active thrusting and folding along the northern Tien Shan and late Cenozoic rotation of the Tarim relative to Dzungaria and Kazakhstan, *J. Geophys. Res.*, *98*, 6755–6804.
- Bennett, E. J., J. Youngson, J. Jackson, R. Norris, G. M. Raisbeck, and F. Yiou (2006), Combining geomorphic observations with in situ cosmogenic isotope measurements to study anticline growth and fault propagation in Central Otago, New Zealand, *N. Z. J. Geol. Geophys.*, *49*, 217–231.
- Burbank, D. W. (2002), Rates of erosion and their implications for exhumation, *Mineral. Mag.*, *66*, 25–52.
- Burbank, D. W., and R. S. Anderson (2001), *Tectonic Geomorphology*, 1st ed., 273 pp., Blackwell Sci., Malden, Mass.
- Burbank, D. W., J. K. McLean, M. E. Bullen, K. Y. Abdrakhmatov, and M. G. Miller (1999), Partitioning of intermontane basins by thrust-related folding, Tien Shan, Kyrgyzstan, *Basin Res.*, *11*, 75–92.
- Butler, R. F. (1992), *Paleomagnetism*, 319 pp., Blackwell Sci., Malden, Mass.
- Cande, S. C., and D. V. Kent (1995), Revised calibration of the geomagnetic polarity timescale for the Late Cretaceous and Cenozoic, *J. Geophys. Res.*, *100*, 6093–6095.
- Cardozo, N., K. Bhalla, A. T. Zehnder, and R. W. Allmendinger (2003), Mechanical models of fault propagation folds and comparison to the trishear kinematic model, *J. Struct. Geol.*, *25*, 1–18, doi:10.1016/S0191-8141(02)00013-5.
- Cartwright, J. A., C. Mansfield, and B. Trudgill (1996), The growth of normal faults by segment linkage, in *Modern Developments in Structural Interpretation, Validation and Modelling*, edited by P. G. Buchanan and D. A. Nieuwland, *Geol. Soc. Spec. Publ.*, *99*, 163–177.
- Charreau, J., Y. Chen, S. Gilder, S. Dominguez, J. Avouac, S. Sen, D. J. Sun, Y. A. Li, and M. W. Wang (2005), Magnetostratigraphy and rock magnetism of the Neogene Kuitun He section (northwest China): Implications for late Cenozoic uplift of the Tianshan mountains, *Earth Planet. Sci. Lett.*, *230*, 177–192.
- Chen, J., G. Qu, J. Shen, E. Sobel, L. Nan, Q. Tian, and J. Yin (2000), Late Cenozoic tectonics along the northwestern margin of the Tarim basin: Interactions between the Tarim basin and the southern Tien Shan, west China, *Earth Sci. Frontiers*, *7*, 323–325.
- Chen, J., D. W. Burbank, K. Scharer, C. Rubin, E. Sobel, G. Qu, J. Shen, J. Yin, and R. Zhao (2001), Late Cenozoic tectonics and seismicity in the southwestern Tien Shan, China, *Earthquake Res. China*, *17*, 134–155.
- Chen, J., D. W. Burbank, K. M. Scharer, E. Sobel, J. Yin, C. Rubin, and R. Zhao (2002), Magnetostratigraphy of the Upper Cenozoic strata in the

- southwestern Chinese Tian Shan: Rates of Pleistocene folding and thrusting, *Earth Planet. Sci. Lett.*, *195*, 113–130.
- Cowie, P. A., S. Gupta, and N. H. Dawers (2000), Implications of fault array evolution for synrift depocentre development; insights from a numerical fault growth model, *Basin Res.*, *12*, 241–261.
- Daéron, M., J.-P. Avouac, and J. Charreau (2007), Modeling the shortening history of a fault tip fold using structural and geomorphic records of deformation, *J. Geophys. Res.*, doi:10.1029/2006JB004460, in press.
- Davis, K., D. W. Burbank, D. Fisher, S. Wallace, and D. Nobes (2005), Thrust-fault growth and segment linkage in the active Ostler fault zone, New Zealand, *J. Struct. Geol.*, *27*, 1528–1546.
- Dawers, N. H., and M. H. Anders (1995), Displacement-length scaling and fault linkage, *J. Struct. Geol.*, *17*, 607–614.
- Demarest, H. H. (1983), Error analysis for the determination of tectonic rotation from paleomagnetic data, *J. Geophys. Res.*, *88*, 4321–4328.
- Elliott, D. (1976), The energy balance and deformation mechanisms of thrust sheets, *Philos. Trans. R. Soc. London*, *283*, 289–312.
- Epard, J.-L., and R. H. Groshong Jr. (1993), Excess area and depth to detachment, *AAPG Bull.*, *77*, 1291–1302.
- Gilder, S., Y. Chen, and S. Sen (2001), Oligo-Miocene magnetostratigraphy and rock magnetism of the Xishuigou section, Subei (Gansu Province, western China) and implications for shallow inclinations in Central Asia, *J. Geophys. Res.*, *106*, 30,505–30,521.
- Gonzalez-Mieres, R., and J. Suppe (2006), Relief and shortening in detachment folds, *J. Struct. Geol.*, *28*, 1785–1807, doi:10.1016/j.jsg.2006.01.07.0001.
- Gupta, S. (1997), Himalayan drainage patterns and the origin of fluvial megafans in the Ganges foreland basin, *Geology*, *25*, 11–14.
- Gupta, A., and C. Scholz (1998), Utility of elastic model in predicting fault displacement fields, *J. Geophys. Res.*, *103*, 823–834.
- Hardy, S., and E. Finch (2005), Discrete-element modelling of detachment folding, *Basin Res.*, *17*, 507–520.
- Hardy, S., and J. Poblet (1994), Geometric and numerical model of progressive limb rotation in detachment folds, *Geology*, *22*, 371–374.
- Heermance, R., J. Chen, K. Schärer, and D. W. Burbank (2004), Tertiary deformation in the Kashgar basin, southern margin of the Tian Shan, China, *Eos Trans. AGU*, *85*(47), Fall Meet. Suppl., Abstract T31E-05.
- Hu, L. Y. (1982), Late Tertiary foraminifera of Tarim Basin and their geological significance, *Chin. Sci. Bull.*, *15*, 938–941.
- Jackson, J., R. Norris, and J. Youngson (1996), The structural evolution of active fault and fold systems in central Otago, New Zealand: Evidence revealed by drainage patterns, *J. Struct. Geol.*, *18*, 217–234.
- Jia, C., S. Zhang, and S. Wu (2004), *Stratigraphy of the Tarim Basin and adjacent areas* (in Chinese with English abstract), 1063 pp., Science Press, Beijing.
- Jones, C. H. (2002), User-driven integrated software lives: “PaleoMag” paleomagnetism analysis on the Macintosh, *Comput. Geosci.*, *28*, 1145–1151.
- Kirschvink, J. L. (1980), The least-squares line and plane and the analysis of paleomagnetic data, *Geophys. J. R. Astron. Soc.*, *62*, 699–718.
- Li, D., D. Liang, C. Jia, G. Wang, Q. Wu, and D. He (1996), Hydrocarbon accumulations in the Tarim basin, China, *AAPG Bull.*, *80*, 1587–1603.
- McElhinny, M. W. (1964), Statistical significance of the fold test in paleomagnetism, *Geophys. J. R. Astron. Soc.*, *8*, 338–340.
- McFadden, P. L., and M. W. McElhinny (1990), Classification of the reversal test in paleomagnetism, *Geophys. J. Int.*, *103*, 725–729.
- Mitra, S. (1990), Fault-propagation folds: Geometry, kinematic development and hydrocarbon traps, *AAPG Bull.*, *74*, 921–945.
- Mitra, S. (2002), Structural models of faulted detachment folds, *AAPG Bull.*, *86*, 1673–1694.
- Mitra, S. (2003), A unified kinematic model for the evolution of detachment folds, *J. Struct. Geol.*, *25*, 1659–1673.
- Poblet, J., and K. McClay (1996), Geometry and kinematics of single-layer detachment folds, *AAPG Bull.*, *80*, 1085–1109.
- Poblet, J., K. McClay, F. Storti, and J. A. Muñoz (1997), Geometries of syntectonic sediments associated with single-layer detachment folds, *J. Struct. Geol.*, *19*, 369–381.
- Qian, Y. X., R. S. Ji, D. Y. Qin, G. X. Liu, and W. L. Pan (2001), An assessment of hydrocarbon potential of Mesozoic-Cenozoic basins in the northern part of Kashi depression of Tarim basin (in Chinese with English abstract), *Pet. Geol. Exp.*, *23*, 32–37.
- Quidelleur, X., and V. Courtillot (1996), On low-degree spherical harmonic models of paleosecular variation, *Phys. Earth Planet. Inter.*, *95*, 55–77.
- Reigber, C., G. W. Michel, R. Galas, D. Angermann, J. Klotz, J. Y. Chen, A. Papschev, R. Arslanov, V. E. Tzurkov, and M. Ishanov (2001), New space geodetic constraints on the distribution of deformation in central Asia, *Earth Planet. Sci. Lett.*, *191*, 157–165.
- Riba, O. (1976), Syntectonic unconformities of the Alto Cardener, Spanish Pyrenees: A genetic interpretation, *Sediment. Geol.*, *15*, 213–233.
- Rockwell, T. K., E. A. Keller, and G. R. Dembroff (1988), Quaternary rate of folding of the Ventura Avenue anticline, western Transverse Ranges, southern California, *Geol. Soc. Am. Bull.*, *100*, 850–858.
- Scharer, K. M., D. W. Burbank, J. Chen, R. J. Weldon, C. Rubin, R. Zhao, and J. Shen (2004), Detachment folding in the southwestern Tian Shan–Tarim foreland, China; Shortening estimates and rates, *J. Struct. Geol.*, *26*, 2119–2137.
- Scharer, K. M., D. W. Burbank, J. Chen, and R. J. Weldon (2006), Kinematic models of fluvial terraces over active detachment folds: Constraints on the growth mechanism of the Kashi-Atushi fold system, Chinese Tian Shan, *Geol. Soc. Am. Bull.*, *118*, 1006–1021.
- Scholz, C. H. (2002), *The Mechanics of Earthquakes and Faulting*, 471 pp., Cambridge Univ. Press, New York.
- Sobel, E. R., and T. Dumitru (1997), Thrusting and exhumation around the margins of the western Tarim basin during the India-Asia collision, *J. Geophys. Res.*, *102*, 5043–5064.
- Sobel, E. R., J. Chen, and R. V. Heermance (2006), Late Oligocene–early Miocene initiation of shortening in the southwestern Chinese Tian Shan: Implications for Neogene shortening rate variations, *Earth Planet. Sci. Lett.*, *247*, 70–81.
- Suppe, J. (1983), Geometry and kinematics of fault bend folding, *Am. J. Sci.*, *283*, 648–721.
- Suppe, J., and D. A. Medwedeff (1990), Geometry and kinematics of fault-propagation folding, *Eclogae Geol. Helv.*, *83*, 409–454.
- Suppe, J., F. Sabat, J. A. Muñoz, J. Poblet, E. Roca, and J. Vergés (1997), Bed-by-bed fold growth by kink-band migration: Sant Llorenç de Morunys, eastern Pyrenees, *J. Struct. Geol.*, *19*, 443–461.
- Taponnier, P., and P. Molnar (1979), Active faulting and Cenozoic tectonics of the Tien Shan, Mongolia and Baykal regions, *J. Geophys. Res.*, *84*, 3425–3459.
- Thompson, S. C., R. J. Weldon, C. M. Rubin, K. Abdrakhmatov, P. Molnar, and G. W. Berger (2002), Late Quaternary slip rates across the central Tien Shan, Kyrgyzstan, central Asia, *J. Geophys. Res.*, *107*(B9), 2203, doi:10.1029/2001JB000596.
- Wang, Q., et al. (2001), Present-day crustal deformation in China constrained by Global Positioning System measurements, *Science*, *294*, 574–577.
- Ward, P. D., et al. (2005), Abrupt and gradual extinction among land vertebrates in the Karoo Basin, South Africa, *Science*, *307*, 709–714.
- Whipple, K., E. Kirby, and S. Brocklehurst (1999), Geomorphic limits to climate-induced increases in topographic relief, *Nature*, *401*, 39–43.
- Willett, S. D., and M. T. Brandon (2002), On steady states in mountain belts, *Geology*, *30*, 175–178.
- Xiao, A. C., C. Jia, S. F. Yang, G. J. Wei, H. L. Chen, and C. Zhang (2000), The kinematics characters of the thrust-fold belts western front regions in southern Tianshan, China (in Chinese with English abstract), *Acta Sedimentol. Sin.*, *18*, 439–444.
- Xinjiang Bureau of Geology and Mineral Resources (1993), *Regional Geology of the Xinjiang Uygur Autonomous Region*, 561 pp., Geol. Publ. House, Beijing.
- Yin, A., S. Nie, P. Craig, and T. M. Harrison (1998), Late Cenozoic tectonic evolution of the southern Chinese Tian Shan, *Tectonics*, *17*, 1–27.
- Zhou, Z. Y., and P. J. Chen (1990), *Biostratigraphy and Geological Evolution in the Tarim Basin*, 439 pp., Geol. Press, Beijing.

D. W. Burbank and R. Heermance, Department of Earth Science, University of California, Santa Barbara, CA 93106, USA.

J. Chen and C. Wang, State Key Laboratory of Earthquake Dynamics, Institute of Geology, China Earthquake Administration, Beijing 100029, China. (chenjie@eq-igl.ac.cn)

J. Miao, Basin and Reservoir Research Center, China University of Petroleum, Beijing 102249, China.

K. M. Schärer, Department of Geology, Appalachian State University, Boone, NC 28608, USA.